coatings

MDPI

Article

Deposition and Rebound Behavior of a Single Particle on Superhydrophobic Surfaces with Ribbed and Random Roughness Structures

Wenjun Zhao [1] and Hao Lu [2,3,4,*]

[1] Department of Architecture and Built Environment, Faculty of Engineering, University of Nottingham, Nottingham NG7 2RD, UK
[2] Laboratory of Energy Carbon Neutrality, School of Electrical Engineering, Xinjiang University, Urumqi 830047, China
[3] Engineering Research Center of Northwest Energy Carbon Neutrality, Ministry of Education, Xinjiang University, Urumqi 830047, China
[4] Key Laboratory of Plateau Oxygen and Living Environment of Xizang Autonomous Region, Xizang University, Lhasa 850000, China
* Correspondence: luhao@xju.edu.cn

Abstract

Particle deposition, rebound, and adhesion on rough surfaces play a crucial role in a wide range of powder handling, aerosol transport, and fouling-related processes. However, the underlying mechanisms governing single-particle interactions with rough surfaces, particularly those with complex surface morphologies, remain insufficiently understood. In this work, the deposition and elastic rebound behavior of an individual particle impacting superhydrophobic surfaces with ribbed and randomly distributed roughness structures are systematically investigated through a combined experimental and numerical approach. A coupled Lattice Boltzmann Method (LBM) and Discrete Particle Model (DPM) was developed, in which a new particle–surface contact model is proposed to account for adhesion, elastic deformation, and localized roughness effects through multi-node interactions. Randomly distributed rough surfaces are reconstructed using a Fast Fourier Transform (FFT)-based method, and single-particle impact experiments are conducted to validate the numerical predictions. Good agreement is achieved between simulated and measured values, with a relative error for the maximum rebound height of only 5.9% and a peak velocity deviation prior to impact of approximately 5.4%. Parametric analyses demonstrate that particle diameter, Young's modulus, surface energy, surface roughness morphology, and flow Reynolds number all influence particle deposition outcomes. Larger particles exhibit significantly higher rebound heights due to increased stored elastic energy; specifically, when particle size increases from 20 μm to 100 μm, the maximum rebound height increases by a factor of 2.1. In contrast, smaller particles are more prone to adhesion after repeated impacts. The rebound height of particles decreases as surface energy increases. When surface energy rises from 0.01 J/m^2 to 0.05 J/m^2, rebound height drops from 53.65% to 38.66%. At 0.5 J/m^2, particles adhere immediately. Compared with ribbed surfaces, randomly distributed rough surfaces promote particle rebound by reducing effective contact area and inducing complex impact orientations. Particle rebound behavior is primarily governed by particle diameter, while material properties such as Young's modulus and surface energy exhibit secondary and nonlinear effects. The proposed model provides a validated and transferable framework for analyzing particle–surface interactions on rough surfaces and offers physical insights relevant to the control of particle deposition in powder and particulate systems.

Check for updates

Academic Editor: Giorgos Skordaris

Received: 25 January 2026
Revised: 3 March 2026
Accepted: 4 March 2026
Published: 6 March 2026

Copyright: © 2026 by the authors. Licensee MDPI, Basel, Switzerland. This article is an open access article distributed under the terms and conditions of the Creative Commons Attribution (CC BY) license.

Keywords: particle deposition; particle–surface interaction; adhesion and rebound; rough surfaces; contact mechanics

1. Introduction

Particle deposition on solid surfaces is a common phenomenon in particle-laden flow systems and has been extensively studied due to its significant impact on flow behavior, transport processes, and surface performance. Previous investigations have shown that particle deposition is strongly influenced by surface roughness characteristics, particle size and shape, as well as flow conditions, leading to complex deposition patterns on realistic surfaces [1–4]. In practical flow configurations, deposited particles may alter local flow structures and near-wall transport processes, further affecting subsequent particle motion and deposition behavior [5–7]. Experimental and numerical studies have also demonstrated that surface structuring, such as riblets or patterned roughness, can enhance or suppress particle deposition by modifying near-wall flow fields and particle–wall interactions [8–10]. These findings highlight the importance of understanding particle deposition mechanisms on non-ideal surfaces in particle-laden flows.

While numerous studies have investigated particle deposition on smooth and rough surfaces, most have focused on simplified geometries and have not fully captured the complexity of particle–surface interactions arising from realistic surface morphologies. Previous work has demonstrated that particle deposition is governed by a combination of flow conditions, particle properties, surface roughness, and particle–surface interaction mechanisms [11–14]. Numerical approaches such as Computational Fluid Dynamics (CFD) and the Lattice Boltzmann Method (LBM) have been widely employed to model fluid–particle transport and deposition behavior. However, these models commonly assume smooth or idealized rough surfaces and simplified contact descriptions, limiting their ability to accurately represent particle adhesion, collision, and rebound processes on rough surfaces with complex micro- and nanoscale features. Recent advances in contact mechanics have employed classical contact theories, such as Hertz [15], Johnson–Kendall–Roberts (JKR) [16], and Derjaguin–Muller–Toporov (DMT) [17], to model particle–surface interactions. These theories are largely formulated for smooth or idealized surfaces and therefore exhibit limited applicability when extended to rough surfaces with complex micro- and nanoscale features. In particular, particle interactions with superhydrophobic surfaces involve a coupled interplay of elastic deformation, adhesion, and surface morphology, which cannot be adequately captured by conventional smooth-surface contact models. Consequently, the development of contact models that explicitly account for surface roughness effects is essential for accurately describing particle impact, rebound, and adhesion on rough surfaces.

In parallel, a wide range of numerical studies have investigated particle deposition and settlement behavior using Computational Fluid Dynamics (CFD), the Lattice Boltzmann Method (LBM), and Molecular Dynamics Simulations (MDS). Almohammed and Breuer [18] proposed a model to analyze adhesion-controlled particle–wall interactions in turbulent particle-laden flows, demonstrating that adhesion strongly influences particle–wall collision frequency, particularly for particles of different sizes. Fang et al. [19] developed a finite element–based particle–wall collision model and reported close agreement with experimental data over a broad range of particle sizes and impact velocities. Hemmati et al. [20] examined particle deposition in a horizontal channel with various roughness geometries and heights under turbulent gas flow, showing that the spacing of roughness elements plays a key role in the deposition of small particles. Recent studies

have demonstrated that wall roughness plays a critical role in regulating particle dynamics and deposition behavior in gas–particle flows. Kartushinsky et al. [21] performed combined experimental and numerical investigations to examine the effects of wall roughness on particle motion in various gas–particle flow configurations, showing that roughness significantly modifies particle trajectories, collision frequency, and near-wall dynamics. Li et al. [22] developed an Eulerian particle deposition model that accounts for particle size distribution, indicating the importance of particle-scale characteristics in accurately predicting deposition behavior. Gong et al. [23] further investigated the regulation mechanism of wall roughness on micron-sized particle deposition in pneumatic conveying bend pipes and demonstrated that roughness-induced flow modification strongly influences particle impaction and deposition patterns. In addition, Abbasi and Mehdizadeh [24] employed direct numerical simulations to elucidate the interplay between turbulent flow characteristics and small particle deposition in wall-bounded flows, emphasizing the role of near-wall turbulence structures in particle transport and deposition.

In recent years, the Lattice Boltzmann Method (LBM) has emerged as an effective numerical approach for investigating gas–solid two-phase flows at the mesoscopic scale. Compared with conventional Computational Fluid Dynamics (CFD) methods, LBM offers distinct advantages in handling complex boundaries, coupling with particle dynamics, and computational efficiency. Several studies have combined LBM with particle-based methods to simulate particle–fluid interactions and deposition behavior. Ahmadian and Zheng [25] employed an LBM–DEM coupling framework to simulate fluid–solid interactions involving irregularly shaped particles. Li et al. [26] developed a coupled LBM–LES–DEM model to resolve particle flow dynamics and aggregation processes in microfluidic systems. Furthermore, Xia et al. [27] proposed a particle-resolved DEM–IMB–LBM framework to capture coupled heat–particle–fluid interactions. Collectively, these studies demonstrate the strong capability of LBM-based coupled frameworks for resolving detailed particle transport, collision, and deposition processes in complex flow environments.

From a particle mechanics perspective, superhydrophobic surfaces provide a representative class of rough substrates for studying particle deposition and detachment. While superhydrophobicity is strictly a wetting property defined by high contact angles, the underlying physicochemical characteristics that enable it, namely low surface energy and hierarchical roughness, also govern dry particle adhesion. Specifically, low surface energy reduces the intensity of van der Waals forces, while surface roughness minimizes the effective contact area between the particle and the wall. Consequently, these surfaces can significantly modify particle adhesion and rebound behavior, making the 'superhydrophobic' designation a relevant proxy for low-adhesion surfaces in dry granular flows. Experimental investigations have shown that superhydrophobic coatings can effectively reduce particle accumulation on solid substrates compared with untreated surfaces [28–30]. Despite these observations, the mechanisms governing particle deposition on superhydrophobic surfaces remain insufficiently understood, particularly with respect to how surface roughness morphology interacts with particle properties and flow conditions to control collision, rebound, and adhesion outcomes. A key challenge in modeling particle deposition on superhydrophobic surfaces lies in accurately describing particle–surface collisions involving rough structures. Classical contact theories, including the Hertz, Johnson–Kendall–Roberts (JKR), and Derjaguin–Muller–Toporov (DMT) models [15–17], were originally developed for smooth or idealized surfaces and therefore exhibit limited applicability when directly extended to rough surfaces with complex geometries. More recent studies have sought to address the limitations of classical contact theories by considering surface roughness and multi-asperity contact effects, providing more realistic frameworks for analyzing particle impact, rebound, and deposition on rough surfaces [31–33]. Subsequent developments,

such as the Muller–Yushchenko–Derjaguin (MYD) model [34] and the Maugis–Dugdale model [35], have improved the description of adhesive contact by incorporating the coupling between elastic deformation and surface forces, but these models remain primarily representative of smooth or equivalent smooth-surface interactions. As a result, existing contact models are generally unable to capture the combined effects of surface roughness morphology, adhesion, and elastic deformation that govern particle impact and rebound on rough superhydrophobic surfaces.

In this study, a combined experimental and numerical investigation is conducted to examine the deposition behavior of a single particle impacting superhydrophobic surfaces with rough structures. Randomly distributed rough surfaces are reconstructed based on Atomic Force Microscopy (AFM) measurements, and a coupled LBM–Discrete Particle Model (DPM) framework is employed to simulate particle transport and collision dynamics. A new particle–surface contact model is proposed to account for adhesion, elastic deformation, and localized roughness effects through multi-node interactions. The model is validated against single-particle impact experiments, and the effects of particle size, Young's modulus, surface roughness structure, and surface energy on particle deposition, rebound height, deformation, and interaction forces are systematically analyzed.

2. Experimental Methodology

2.1. Fabrication of Superhydrophobic Coating

The substrate used in the experiment was a glass sample coated with a superhydrophobic coating. The coating was fabricated using the following method. First, organic silicon resin, ethanol, and SiO_2 nanoparticles were mixed for 3 h to prepare the superhydrophobic material. The resulting material was then evenly applied to the clean glass surface. Prior to coating, the glass sample was cleaned with distilled water for 10 min. After applying the coating, the glass sample was dried at 30 °C for 3 h. The selected values for surface energy, Young's modulus, and roughness parameters are typical of materials used in superhydrophobic coatings, such as those applied in microfluidic devices and anti-fouling surfaces. These values are consistent with those found in similar studies and ensure that the model is representative of practical applications. For comparison, an uncoated glass sample was used to assess the impact of the superhydrophobic coating on particle deposition reduction. Once the superhydrophobic coatings were prepared, the contact angle of the glass sample was measured. The results indicate that the contact angle of the coated glass exceeded 150°, confirming the superhydrophobic nature of the coatings. Additionally, AFM images revealed a rough surface with randomly distributed structures. In contrast, the contact angle of the bare glass without coating was found to be less than 50°, indicating that the surface was not superhydrophobic. Therefore, the superhydrophobic coating applied in this experiment effectively enhanced the surface's hydrophobicity.

During coating fabrication, the mixture composition and coating procedure (mixing time, solvent content, and drying conditions) were kept identical for all samples to minimize variability in coating thickness and nanoparticle distribution. The coating thickness and nanoparticle size distribution were not independently quantified in the present work; however, visual inspection indicated a uniform coating coverage at the macroscopic scale.

2.2. Experimental Setup

A particle was released from a predetermined height and impacted the superhydrophobic surface. The experiment was performed at room temperature (30 °C). Particle behavior on the surface was captured using a high-speed camera (PCO.dimax S1). The video recordings allowed for the measurement of the particle's velocity and height, offering insight into the superhydrophobic coating's effectiveness in enhancing particle rebound. Furthermore,

the effects of various factors, including particle size, Young's modulus, surface energy, and surface roughness, on particle deposition were analyzed during the experiment. The main specifications of the camera are shown in Table 1. The particle velocity was calculated using the finite difference method of successive frames. According to standard error propagation analysis, the relative uncertainty in velocity measurement is estimated to be below 3%. Additionally, the camera exhibits excellent linearity (<0.5% differential, <0.2% integral), which further ensures measurement reliability. Each experiment was repeated five times, and the standard deviation of measured impact velocity remained within 3%.

Table 1. PCO High-Speed Camera Model Specifications.

Parameter	Value
Resolution	1008 × 1000 pixels (1 MP)
Pixel size (sensor)	11 µm
Frame rate (at full resolution)	4467 fps
Shutter speed	1.5 µs; 40 ms (adjustable)
Dynamic range	12-bit
Signal-to-noise ratio (SNR)	64 dB
Linearity	<0.5% (differential)/<0.2% (integral)

2.3. Characterization of the Rough Surfaces

The roughness of the superhydrophobic coating surface was characterized using Atomic Force Microscopy (AFM). AFM measurements were performed at multiple locations on each sample to improve representativeness. The roughness parameters (*Sk*, *K*, and *Rq*) are reported as mean values based on 8 scan areas. The parameters of the surface roughness are listed in Table 2. The specific surface profile of the experimental sample can be seen in Figure 1. The reconstruction process will be explained in the following section.

Table 2. Roughness parameters of the superhydrophobic coating.

Sk	*K*	*Rq*/µm
0.351	3.23	0.0513

After measuring the rough surface structures using AFM, parameters such as kurtosis (*K*), skewness (*Sk*), and root mean square (*Rq*) were observed. Such quantitative surface characterization is important because processing conditions (contact-induced heating and tool–surface interactions) can significantly influence the resulting surface quality and topographical features, which in turn affect interfacial contact behavior [36]. These parameters are key in characterizing the rough surface. Skewness describes the symmetry of the surface; a value of 0 indicates a Gaussian distribution. Negative skewness corresponds to a surface with deep valleys and low peaks, while positive skewness suggests higher peaks and shallower valleys. Higher skewness values indicate greater asymmetry in the surface structure. Kurtosis, which describes the surface's steepness, is 3.0 for a Gaussian distribution. If the surface distribution is smoother than a Gaussian, the kurtosis value will be less than 3.0, while a sharper distribution results in a kurtosis greater than 3.0. A higher kurtosis value suggests a greater tendency for the surface to form deep valleys or sharp peaks. Standard deviation quantifies how the surface height deviates from the mean. To accurately reproduce physical topography in numerical simulations, this study reconstructed a randomly rough surface using a method based on the FFT, with actual AFM measurement data as input. This approach ensures that the generated numerical surfaces exhibit high consistency with experimentally measured surfaces in terms of statistical properties (first- and second-order statistics).

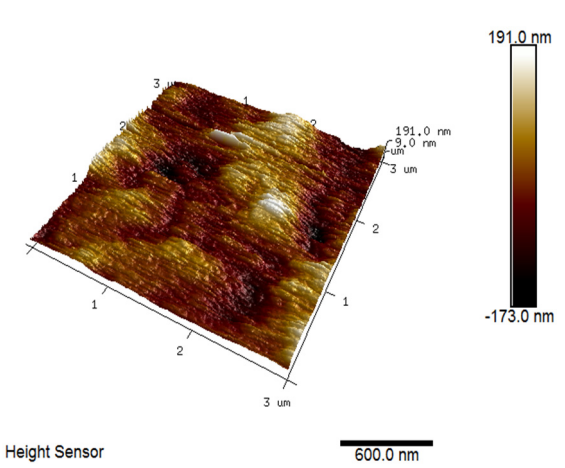

(**a**) 3D surface topography obtained by AFM

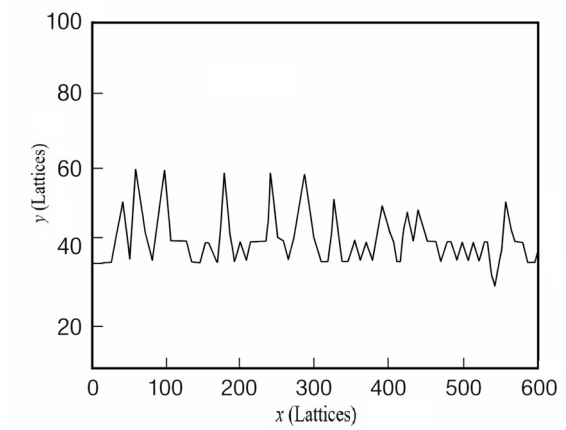

(**b**) 2D cross-sectional surface by reconstruction

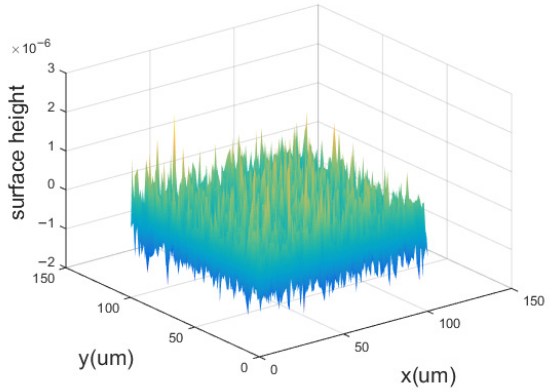

(**c**) 3D surface topography by reconstruction.

Figure 1. Profile of the glass sample surface.

3. Numerical Method

3.1. Lattice Boltzmann Model for the Airflow

The Lattice Boltzmann Method (LBM) is a powerful tool for simulating complex flows, including those in porous media, thermal flows, reactions, mass transfer, turbulence, and multiphase systems. In this study, LBM was utilized to calculate fluid flow. The governing LBM equations are as follows:

$$f_i(x + e_i\delta_t, t + \delta_t) - f_i(x, t) = -\frac{1}{\tau}[f_i(x, t) - f_i^{eq}(x, t)] + F_t \cdot \delta_t \quad (1)$$

where $f_i(x, t)$ denotes the fluid density distribution function and τ represents the relaxation time. The F_t refers to the additional external force. The left side of the equation represents the streaming step, while the right side corresponds to the collision step. The D2Q9 and D3Q19 models are commonly used for LBM simulations. For computational efficiency and accuracy, the D2Q9 model was selected for this study. In the D2Q9 model, the equilibrium distribution function $f_i^{eq}(x, t)$ is given by:

$$f_i^{eq}(x, t) = \rho w_i[1 + \frac{e_i u^{eq}}{Cs^2} + \frac{(e_i u^{eq})^2}{2Cs^4} - \frac{(u^{eq})^2}{2Cs^2}] \quad (2)$$

The weight coefficient w_i is different for different directions. The values of w_0, $w_{1–4}$ and $w_{5–8}$ are 4/9, 1/9 and 1/36, respectively. The discrete velocity of the nodes is given as follows:

$$e_i = \begin{cases} (0,0) & i = 0 \\ c \cdot \left(\cos\left[(i-1) \cdot \frac{\pi}{2}\right], \sin\left[(i-1) \cdot \frac{\pi}{2}\right]\right) & i = 1–4 \\ \sqrt{2} \cdot c \cdot (cos[(2i-1) \cdot \frac{\pi}{4}], sin(2i-1) \cdot \frac{\pi}{4}]) & i = 5–8 \end{cases} \quad (3)$$

The fluid density and the velocity at each node can be calculated by

$$\rho = \sum_i f_i, \quad (4)$$

$$\rho u = \sum_i e_i f_i. \quad (5)$$

The computational domain consists of a uniform Cartesian lattice of 1000 × 1000 nodes. In the present LBM framework, the surface roughness geometry is directly embedded into the fixed lattice grid rather than using a body-fitted mesh. The lattice resolution was selected such that the particle geometry and reconstructed roughness morphology are adequately represented within the domain. Considering that the RMS roughness amplitude (Rq = 0.0513 μm) is significantly smaller than the particle diameter (250 μm), the selected resolution ensures that the essential contact-scale geometry and rebound dynamics are properly resolved. The particle diameter corresponds to approximately 40 lattice units, ensuring sufficient geometric resolution. Furthermore, the close agreement between numerical predictions and experimental measurements (relative error < 6%) provides indirect validation of the adequacy of the chosen lattice resolution.

3.2. Discrete Particle Model for Particle Motion Calculation

In this study, the particle was modeled as a circular object. The particle trajectories were obtained using the Discrete Particle Model based on Newton's second law. The equation of motion for the particle is given as:

$$\frac{dX_p}{dt} = v_p \quad (6)$$

$$m_p \frac{dv_p}{dt} = F_d + mg + F \quad (7)$$

where X_p, v_p are the location and velocity of the particle center, respectively. F_d is the drag force exerted on the moving particle in the fluid flow. F is the contact force between particle and rough surface with randomly distributed structure.

In this paper, the diameter of particles ranges from 20 to 100 μm; thus the drag force exerted on the particles is dominated by viscous drag and the Brownian force can be ignored. The equation for calculating the drag force can be described as:

$$F_d = m_p \frac{1}{\tau} \frac{C_d \, Re_p}{24} (u_g - u_p) \quad (8)$$

where C_d is the drag coefficient and it is different for different Reynolds numbers. As for $\mathrm{Re}_p < 1$, it can be calculated by:

$$C_d = \frac{24}{Re_p} \quad (9)$$

As for larger Reynolds number ($1 < Re_p < 400$), it can be described as:

$$C_d = \frac{24}{Re_p}(1 + 0.15{Re_p}^{0.687}) \tag{10}$$

The particle relaxation time τ can be calculated by

$$\tau = \frac{Sd_p^2 C_c}{18v} \tag{11}$$

where S is the density ratio of the particle to the fluid. C_c is the Cunningham slip correction factor which can be calculated by

$$C_c = 1 + Kn\left(1.257 + 0.4e^{-1.1/Kn}\right) \tag{12}$$

where $K_n = 2\lambda/d_p$ is the Knudsen number, λ = 65 nm is the average free path of air molecules. d_p is the diameter of the particle [37,38]. u_g and u_p are the velocity of fluid and particle center, respectively. The u_g can be calculated based on the average velocity of the eight closest nodes around the particle [39]. F is the contact force between the particle and rough surface with regularly or randomly distributed structure. However, the surfaces are not smooth on the superhydrophobic coatings. Thus, a new kind of contact model was proposed for simulating the particle impacting rough surface. The model would be introduced in the following part.

Applicability range: the present LBM–DPM simulations and validations focus on particle diameters in the range of 20–100 μm, with surface RMS roughness (Rq) much smaller than the particle diameter ($Rq/d_p \ll 1$ in the present coating), and particle Reynolds numbers in the range $Re_p \lesssim 400$ (consistent with the drag correlations adopted in Equations (9) and (10)). Outside these ranges (e.g., very large roughness amplitude comparable to d_p, or higher Re_p requiring different drag/flow treatment), additional validation and/or model extensions would be required.

3.3. Reconstruction of Rough Surface

The reconstruction of regularly distributed rough surfaces can be achieved based on surface structural parameters, such as the height and spacing of the roughness. Figure 1 illustrates one example of a regularly distributed structure. However, randomly distributed rough surfaces are more challenging to define. These surfaces can be obtained in two ways: one is through experimental observation using an atomic force microscope (AFM), and the other is via computational reconstruction. In addition to matching first-order height statistics (Sk, K, and Rq), the present reconstruction procedure explicitly preserves the spatial frequency content of the measured AFM surface. This is achieved by prescribing an exponential autocorrelation function (ACF) with characteristic correlation lengths in the lateral directions. Since the power spectral density (PSD) is the Fourier transform of the ACF, enforcing the target ACF inherently ensures that the reconstructed surface reproduces the corresponding spatial-frequency distribution of the real surface. Therefore, both amplitude statistics and spectral characteristics of the AFM-measured roughness are consistently represented in the numerical surface. This methodology follows standard FFT-based surface reconstruction approaches reported in previous studies [40–42]. The specific reconstruction process using FFT is detailed in the following section.

The rough surface with randomly distributed structure can be characterized in terms of an exponential Auto-Correlation Function and height distribution. The area is represented by $N \times M$ and height arrays $z(I, j)$. It is sufficient to reconstruct the randomly distributed rough surface by using the first four statistical moments of the height array $z(I, j)$. These

moments correspond to the average, root mean square roughness, skewness, and kurtosis, respectively. The mean is 0 while the three moments are the values associated with the arrays. The four statistical moments and an exponential ACF (R_z) are expressed as follows:

$$\bar{z} = \frac{1}{MN}\sum_{j=0}^{M-1}\sum_{i=0}^{N-1} z_{ij} \tag{13}$$

$$R_q{}^2 = \frac{1}{MN}\sum_{j=0}^{M-1}\sum_{i=0}^{N-1} z_{ij}{}^2 \tag{14}$$

$$Sk = \frac{1}{MNR_q{}^3}\sum_{j=0}^{M-1}\sum_{i=0}^{N-1} z_{ij}{}^3 \tag{15}$$

$$K = \frac{1}{MNR_q{}^4}\sum_{j=0}^{M-1}\sum_{i=0}^{N-1} z_{ij}{}^4 \tag{16}$$

$$R_z(k,l) = R_q{}^2 exp[-2.3\sqrt{(\frac{k}{\beta_x})^2 + (\frac{l}{\beta_y})^2}] \tag{17}$$

where l = 1, 2, …, M and k = 1, 2, …, N. β_x and β_y are the auto-correlation lengths of the surface in the x and y directions, respectively. If $\beta_x = \beta_y$, the surface is isotropic. Equations (13)–(16) provide information about the rough surface structure in the vertical direction, while Equation (17) controls the distribution in the horizontal direction.

Randomly distributed rough surfaces with varying skewness and kurtosis values for a given R_q and β are generated using a 2D digital filter technique proposed by Hu and Tonder [43]. The sequence $z(I, j)$ with an amplitude distribution can be obtained by an input sequence $\eta(I, j)$ with the filter function $h(k, l)$. The filter function $h(k, l)$ represents a linear transformation. The transformation system described as:

$$z(i,j) = \sum_{k=1}^{N}\sum_{l=1}^{M} h(k,l)\eta(i+k-\left\lceil\frac{i+k}{N}-1\right\rceil N, j+l-\left\lceil\frac{i+k}{N}-1\right\rceil M) \tag{18}$$

where j = 1, 2, …, M, and i = 1, 2, …, N. h is a digital filter function. The symbol ⌈ ⌉ is referred to obtain the smallest integer.

The filter function $h(k, j)$ represents the relation between the $\eta(i, j)$ and the real roughness $z(i, j)$. In order to obtain $h(k, j)$, some computational steps were necessary:

Firstly, Equation (18) is taken into Fourier transform, as follows,

$$Z(I,J) = H(I,J)A(I,J) \tag{19}$$

where I = 1, 2, …, N and J = 1, 2, …, M. $A(I, J)$ and $Z(I, J)$ are the output of the Fourier transforms of η and z, respectively. $H(I, J)$ is the transfer function of the system, given by

$$H(I,J) = \sum_{k=1}^{N}\sum_{l=1}^{M} h(k,l)e^{-jk\omega_x}e^{-jk\omega_y} \tag{20}$$

where $\omega_x = 2\pi I/N$, $\omega_y = 2\pi J/M$, representing the discrete spatial frequencies.

Next, the probability density function of the rough surface is obtained by performing a Fourier transform on the auto-correlation function.

$$S_z(I,J) = \sum_{k=1}^{N}\sum_{l=1}^{M} R_z(k,l)e^{-jk\omega_x}e^{-jk\omega_y} \tag{21}$$

Since the input sequence η(i, j) is random, the probability density function S_η is 1.0. For a linear system, the relationship between S_η and S_z is as follows:

$$S_z(I,J) = |H(I,J)|^2 S_\eta(I,J) \tag{22}$$

The $H(I, J)$ can be obtained by Equations (19) and (20). $h(k, l)$ can be calculated as:

$$h(k,l) = \frac{1}{MN}\sum_{I=1}^{N}\sum_{J=1}^{M} H(I,J)e^{jk\omega_x}e^{jl\omega_y} \tag{23}$$

Using Equation (18), the function $h(k, l)$ enables the calculation of $z(i, j)$, thereby producing Gaussian-type random surfaces. In practice, however, the height distribution of rough surfaces with randomly distributed features often deviates from a Gaussian profile. Therefore, the initial sequence $\eta(i, j)$ needs to be converted into a non-Gaussian sequence η' as described in Refs. [44,45]. The specific transformation can be seen in the literature [46,47].

(1) Accordingly, rough surfaces containing stochastic structural variations can be reconstructed through the following procedure:
(2) Measure the *Sk*, *K*, and *Rq* values from the real rough surface.
(3) Use a random number generator to create a Gaussian input sequence $\eta(i, i)$.
(4) Transform the input sequence $\eta(i, j)$ to the non-Gaussian sequence $\eta'(i, j)$ based on the Johnson translator system.
(5) Calculate the filter function $h(k, l)$ by using Equations (17)–(23).
(6) The final rough surface $z(i, j)$ is then obtained through Equation (18).

In this paper, to reconstruct the rough surface, the *Sk*, *K*, *Rq* of the actual surface are used. The glass sample in Table 2 is reconstructed. The skewness, kurtosis and *Rq* are 0.351, 3.23 and 0.051, respectively. Although the roughness amplitude is much smaller than the particle diameter, the local asperity-scale contacts significantly modify the effective contact area and impact orientation, thereby influencing rebound behavior.

3.4. The New Contact Force Model Between the Particle and Superhydrophobic Surface

In contrast to classical smooth-surface contact formulations, the rough morphology of superhydrophobic coatings leads to multiple localized contacts and spatially varying impact orientations. Therefore, a new multi-node contact model is developed to simulate particle impact, rebound, and adhesion on rough surfaces. This local application of the JKR theory has been widely adopted in multi-asperity and rough-surface contact modeling, where each asperity is treated as an equivalent smooth contact. For computational efficiency, several assumptions are introduced:

1. Only normal forces are considered between the particle and the rough surface, while the tangential force effects are neglected.
2. The influence of friction is not considered during the collision between the particle and the rough surface.
3. The rough structure of the surface is assumed to remain intact when the particle deposits on it.

Unlike the traditional JKR model, which assumes a single point of contact, or DEM JKR models that employ multiple inequalities over discrete contact regions, the proposed model evaluates adhesion at each localized node of the surface. This allows for a more accurate representation of contact dynamics, particularly for rough surfaces, where multiple asperity-scale contacts significantly influence particle rebound behavior.

In this study, the contact model focuses on the normal interaction between the particle and the rough surface, while tangential forces, friction, and particle rotation are not

explicitly calculated. This simplification is physically justified for the micron-sized adhesive particles (20–100 μm) investigated here, where the collision dynamics are primarily governed by the interplay between strong van der Waals adhesive forces and elastic deformation in the normal direction. As noted in the previous literature [39], particle sliding is relatively rare for small adhesive particles during the brief impact duration, rendering the sliding force negligible compared to the dominant normal trapping forces. Furthermore, the primary objective of this work is to isolate the influence of surface morphology, specifically how roughness slope and frequency alter the effective contact area and impact orientation, rather than the frictional dissipation mechanisms. Consequently, while the exclusion of friction may lead to a conservative estimation of energy loss and a slight over-prediction of absolute rebound heights, the relative trends regarding the efficacy of random versus regular roughness in suppressing deposition remain valid due to the geometric reduction in effective contact area.

A revised contact model is established to evaluate the interaction forces between the particle and the rough surface. First, computational domain of the rough surface, with both regularly and randomly distributed structures, is discretized into grid nodes. Each node is represented by a set of coordinates, and these nodes serve as the numerical representation of the solid surface throughout the computation. Next, the separation between the particle center and the surface-representing nodes is obtained from their respective coordinates. This distance is then used to determine whether the particle interacts with the rough surface. When the distance is smaller than the particle radius, contact is considered to occur. The JKR model is subsequently applied to compute the resulting contact force based on this separation. Accordingly, the contact force acting on the particle is evaluated as follows:

$$F = \sum_{1}^{Nt} F_n \tag{24}$$

$$F_n = F_{ne} + F_{nd} \tag{25}$$

where F_n is the contact force of each contact node, F is the total force obtained by the rough surface. N_t is the number of the contact node. F_{ne} is the elastic force caused by the particle deformation while F_{nd} is the dissipation force during the collision process. The multi-node interaction model ensures that adhesion forces are computed independently at each localized contact point. This prevents the overestimation of adhesive forces, which can occur in models that treat the entire contact area as a single node. By calculating forces at each asperity, our model provides a more accurate representation of adhesion. Therefore, the contact force between the particle and rough surface can be calculated according to Equations (24) and (25). For the F_{ne} and F_{nd}, the JKR model can be adopted for the calculation. The elastic force F_{ne} can be modified due to the van der Waals force and calculated by

$$\frac{F_{\mathrm{ne}}}{F_c} = 4\left(\frac{a}{a_0}\right)^3 - 4\left(\frac{a}{a_0}\right)^{3/2} \tag{26}$$

$$\frac{\delta n}{\delta c} = 6^{1/3}\left[2\left(\frac{a}{a_0}\right)^2 - \frac{4}{3}\left(\frac{a}{a_0}\right)^{1/2}\right] \tag{27}$$

In the equation, δ_n denotes the normal overlap between particles and contact nodes. δ_c represents the critical overlap while the F_c is the critical force. a_0 is the contact region radius at equilibrium during the collision process. The system reaches equilibrium when the elastic response of the contacting surfaces is matched by the adhesive forces pulling them together.

$$\delta n = r_i - \left| X_i - X_j \right| \tag{28}$$

$$\delta c = \frac{a_0^2}{2(6)^{1/3} R} \tag{29}$$

$$a_0 = \left(\frac{9\pi\gamma(R)^2}{E}\right)^{1/3} \tag{30}$$

The F_c can be calculated by

$$F_c = 3\pi\gamma R \tag{31}$$

The dissipation force F_{nd} can be calculated by

$$F_{nd} = -\eta_n v_{pr} \cdot n \tag{32}$$

$$v_p = v_{pi} + w_{pi} r_{pi} \tag{33}$$

where v_p is the particle relative velocity. η_n is the normal dissipation coefficient during the collision. It can be calculated by

$$\eta_n = \alpha (m_p k_N)^{1/2} \tag{34}$$

where α is the coefficient of friction which can be regarded as a function of restitution coefficient of the particles. k_N is the elastic stiffness which is related to the contact radius and it can be described as

$$k_N = \frac{4}{3} E a \tag{35}$$

Thus, the F_n consisting of F_{ne} and F_{nd} can be calculated based on the above model. In this study, particle sliding is pretty rare for small adhesive particles moving and the sliding force can be neglected [39]. Therefore, the contact force F acting between the particle and the rough surface can be subsequently determined. The advantage of proposed computational model is that it is not necessary to consider the specific contact between the particle and the rough surface. The nodes contacting with the particle are used to replace the surface impacts with the particle. This model can be used to calculate the single particle colliding with the rough surface. The airflow is simulated using the Lattice Boltzmann method, and the computational domain is discretized into cells. Therefore, the new contact theory model can be used based on the divided cells. The contact force between the particle and the rough surface is accurately resolved in this study.

In this study, the physical time steps differ between the particle sedimentation and surface collision processes. The time step for sedimentation is longer, while a shorter time step is applied as the particle approaches the surface. Upon contacting a node representing the surface, the particle experiences significant changes in its motion state, which may prevent further contacts with other nodes. The proposed numerical model is capable of simulating particle deposition characteristics on rough surfaces with both regular and random structures. Although the JKR theory is originally derived for smooth contacts, its local application at individual asperity-scale contact nodes has been shown to provide a reasonable approximation under the assumption that local asperity contacts can be treated as equivalent smooth contacts.

To systematically elucidate the core differences between the multi-node JKR contact model proposed in this paper and other representative rough surface contact methods, we conducted a comparative analysis across four aspects. The results are summarized in Table 3. Greenwood Williamson type models describe rough contact statistically via an asperity-height distribution and typically predict macroscopic contact area/force re-

lationships, whereas the present approach resolves contact locally on the LBM lattice by detecting all surface nodes within the particle radius and computing node-wise JKR forces. Compared with previously published LBM-DEM rough-contact implementations that often approximate roughness through effective restitution/roughness parameters or simplified wall functions, the proposed model provides an explicit node-resolved adhesion-elastic response that naturally couples to the same discretization used for LBM-DPM, enabling sub-grid roughness to influence impact orientation, effective contact area, and rebound dynamics.

Table 3. Comparison with representative rough-surface contact approaches.

Item	GW-Type Multi-Asperity (Statistical)	DEM Multi-Contact JKR (Constraints)	Prior LBM-DEM/LBM-DPM Rough Contact (Typical)	This Work: Multi-Node JKR on LBM Lattice
Roughness representation	Asperity statistics (no explicit geometry)	Explicit geometry/contacts (DEM-based)	Often effective roughness/restitution or simplified geometry	Explicit regular + FFT-reconstructed roughness on grid
Contact/adhesion computation	Macroscopic averaged contact; adhesion often effective	JKR per contact pair; multi-contact management needed	Collision rules often simplified; adhesion not always node-resolved	Node-wise JKR at all contacting surface nodes
Coupling to flow discretization	Not grid-coupled	Not inherently tied to LBM lattice	Coupled to LBM but rough contact may be closure-based	Grid-consistent: contact nodes coincide with LBM discretization
What it captures best	Mean load-area trends	Detailed DEM collision kinematics	Transport + deposition trends	Sub-grid roughness effects on effective contact area, local normals, rebound orientation/height

4. Numerical Validation

The numerical model was validated through experimentation. In the experiment, a particle was released from a specified height with an initial velocity of 0, and it subsequently collided with the glass sample. The parameters and values for the particle and fluid used in the experiment are provided in Table 4. For the numerical simulation, the computational domain was set to 1000 × 1000. Additionally, considering the influence of the rough surface structure, the parameters for surface reconstruction are also described.

Table 4. Experimental and numerical simulation parameters and values.

Particle		Fluid Phase		Surface	
Density (kg/m^3)	2500	Viscosity (Pa·s)	1.8×10^{-5}	Sk	0.351
Diameter (m)	250×10^{-6}	Density (kg/m^3)	1.29	K	3.23
Young's modulus (MPa)	100	Cavity Height(m)	1.0×10^{-2}	R_q	0.0513
Released height (m)	4.612×10^{-3}	Cavity Width(m)	1.0×10^{-2}	Surface energy (J/m^2)	0.068

Figure 2 shows the particle deposition process recorded in the experiment using a high-speed camera. The simulation results for particle deposition on the superhydrophobic surface, presented in Figure 3, are in good agreement with the experimental observations. The particle's velocity and height at different time intervals can be seen in Figure 3, with

experimental data obtained from the high-speed camera. Figure 3 compares the simulated particle velocity and height with experimental data. To quantify the agreement, the relative error for the maximum rebound height was calculated. The experimental rebound height was measured at approximately 2.85 mm, while the numerical prediction was 3.02 mm, resulting in a relative error of 5.9%. Similarly, the deviation in peak velocity prior to impact was found to be approximately 5.4% (Experimental: 0.28 m/s vs. Simulation: 0.295 m/s). These quantitative indicators confirm that the proposed multi-node contact model captures the energy dissipation and rebound dynamics with reasonable accuracy.

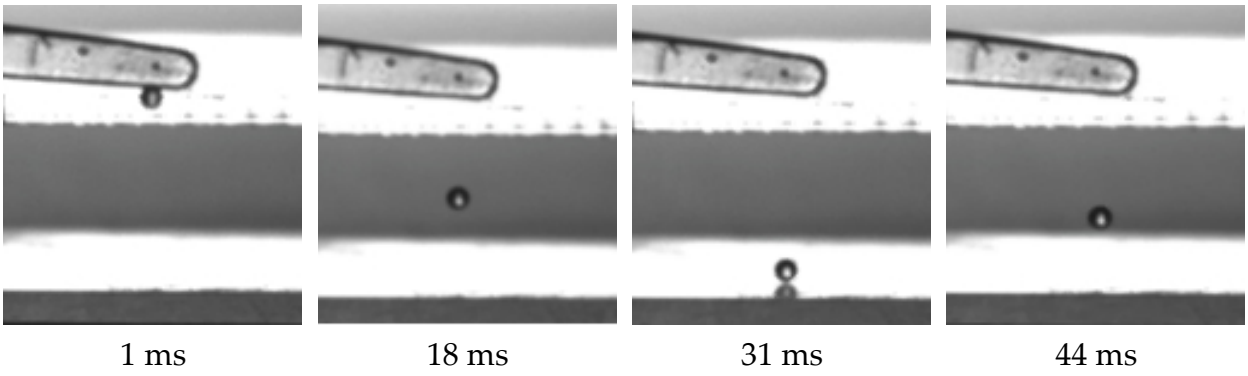

Figure 2. Particle deposition behaviors in the experiment.

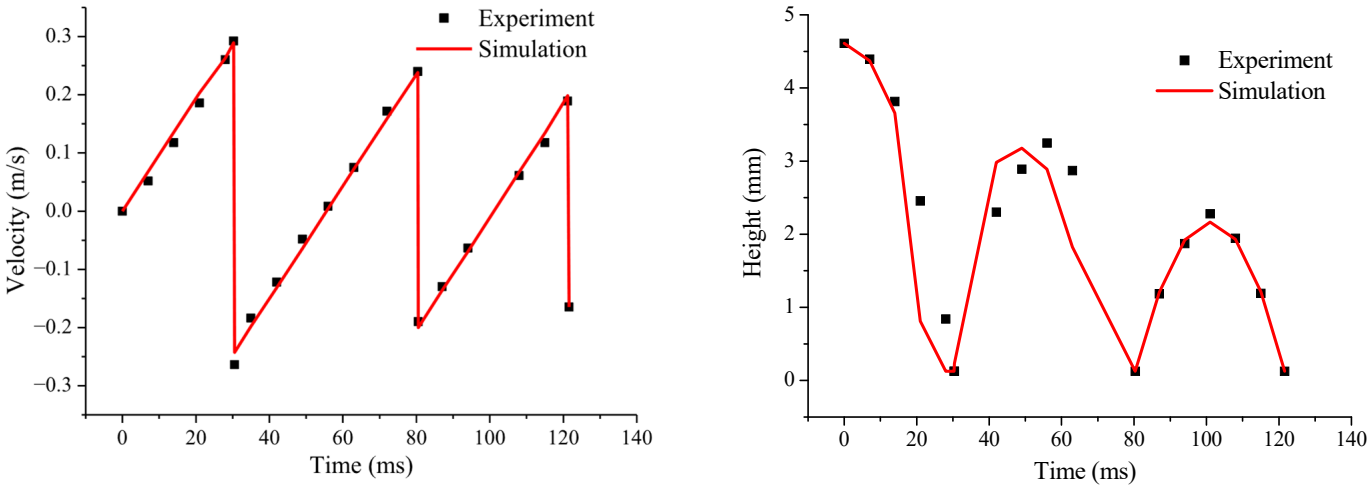

(**a**) Particle velocity (**b**) Particle Height

Figure 3. Comparison of the particle velocity and height between the experiment and simulation.

The minor discrepancies observed between the experimental and numerical results can be attributed to both experimental and numerical uncertainties. The experiments were repeated 5 times under identical conditions to ensure repeatability, showing consistent rebound trajectories with a standard deviation of less than 3% in rebound height. However, measurement uncertainty persists due to the spatial resolution of the high-speed camera (PCO.dimax S1) and slight variations in the initial particle release mechanism. On the numerical side, the particle is modeled as a perfect sphere, whereas the actual experimental particles may exhibit slight non-sphericity. Furthermore, the drag coefficient (C_d) calculations rely on standard correlations (Equations (9) and (10)) which may introduce slight deviations in the instantaneous velocity predictions during the acceleration phase. Despite these factors, the observed relative errors (<6%) fall within the range of combined exper-

imental and numerical uncertainty, validating the reliability of the model for predicting deposition on rough surfaces.

During settling, the particle initially accelerates, but the acceleration decreases due to the drag force from the airflow. Upon colliding with the rough surface, the particle rebounds, with a brief total contact time. After rebounding, the particle moves upward before descending to collide with the surface again. To evaluate the effect of the superhydrophobic surface on rebound behavior, a bare glass surface was used for comparison. As shown in Figure 4, the superhydrophobic coating significantly enhances particle rebound, resulting in higher rebound heights compared to the bare glass. These findings validate the proposed sedimentation-collision model, demonstrating its ability to predict particle deposition on both rough and smooth surfaces. The superhydrophobic coating effectively increases the particle's rebound velocity and height relative to the bare glass.

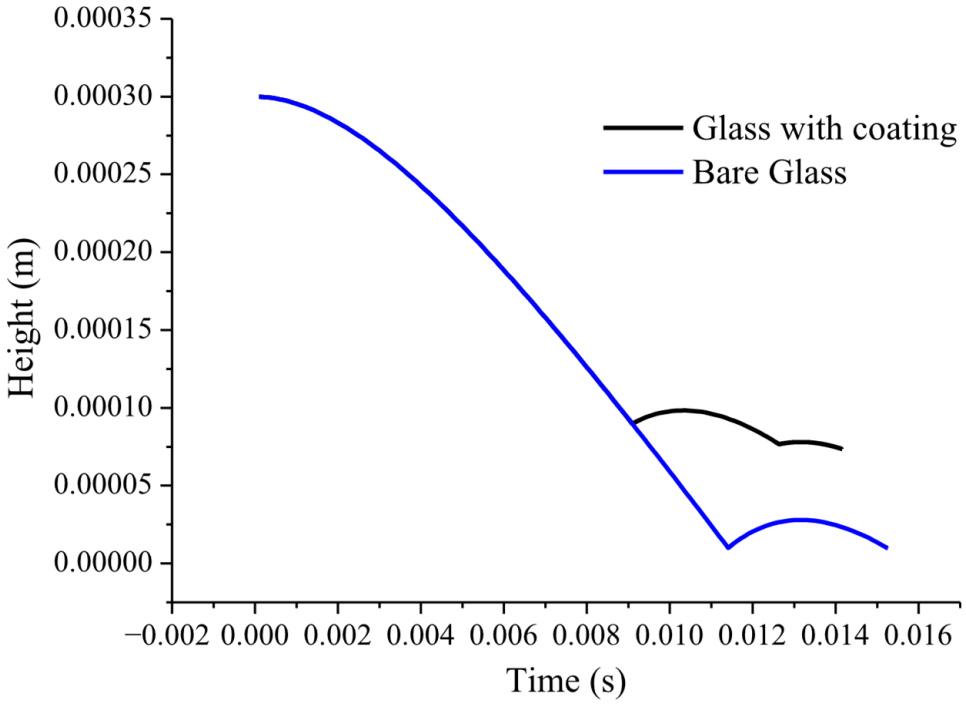

Figure 4. The rebound height of the particle deposition on different surfaces.

5. Computational Cases

This study investigates the influence of particle size, Young's modulus, surface energy, and surface roughness on particle deposition characteristics. The particle's position, velocity, deformation, and the external forces acting on it were computed individually. The computational setup is as follows: a particle enters a microchannel with air flowing at a specified velocity. The left boundary of the domain is defined as a velocity inlet, while the right boundary is set as a fully developed flow outlet. The top and bottom boundaries are assigned no-slip conditions. Since $Kn \ll 1$, the continuum assumption is valid. The bottom surface, featuring either regularly or randomly distributed rough structures, is similarly treated with a no-slip condition. For nodes occupied by the particle or the rough surface, the velocity is set to zero. A schematic of the computational domain is presented in Figure 5.

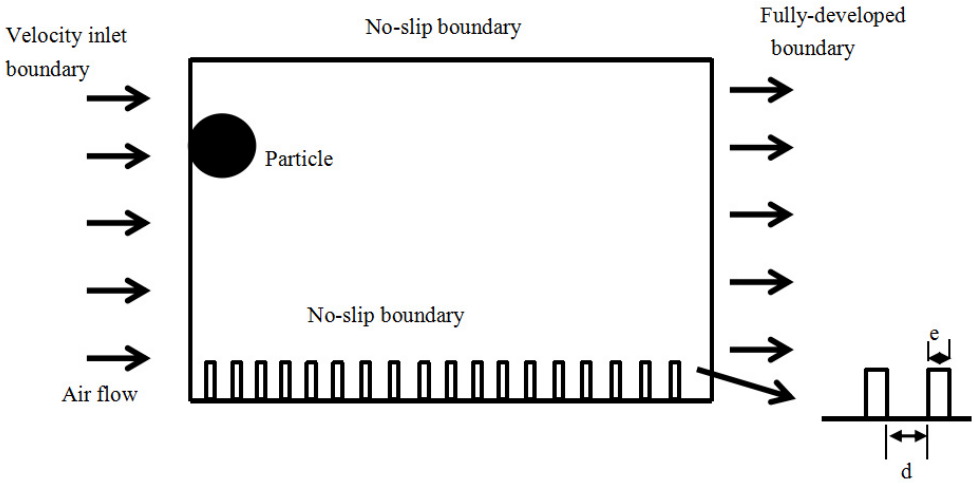

(**a**) Surface with regularly distributed structures

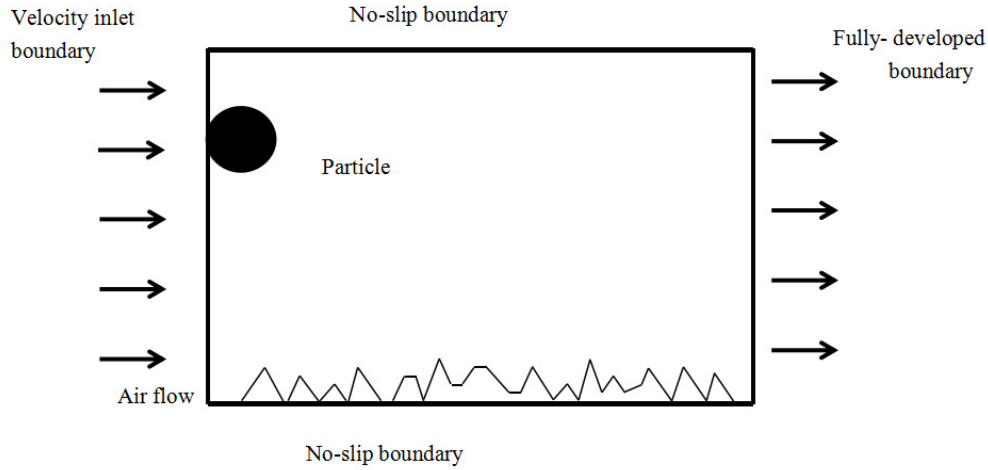

(**b**) Surface with randomly distributed structure

Figure 5. Schematic of the computational cases.

6. Results and Discussions

6.1. Effects of Particle Diameter

Investigating the deposition and rebound behavior of particles of varying sizes in microchannels with superhydrophobic surfaces is of significant importance. In this study, a superhydrophobic surface with a regularly distributed structure was used to simulate the effects of particle diameter on deposition behavior. The particle height, velocity, deformation, and external forces on the particle at different times were analyzed in detail.

As shown in Figure 6a, it is evident that the rebound height of larger particles is higher than that of smaller particles. The highest rebound heights are 19.1%, 53.7%, and 59.3% of the initial height for particles with diameters of 20 μm, 50 μm, and 100 μm, respectively. This indicates that larger particles are more likely to rebound off the surface. For the 20 μm diameter particle, it adheres to the surface immediately after the second impact, whereas larger particles can rebound multiple times. This is because the potential energy of the larger particles is greater than that of the smaller ones. When the larger particle contacts the surface, the stored elastic and plastic energy from its potential energy exceeds the adhesion energy, allowing the particle to rebound. In contrast, the stored energy in the smaller particle is less than the adhesion energy, causing it to adhere to the surface [48].

Larger particles generally undergo multiple rebounds upon surface contact. However, their rebound height decreases with successive impacts, while the number of rebounds

increases. This behavior results from the combined effects of drag force, contact force, and velocity dissipation during deposition. Consequently, larger particles achieve higher rebound heights, whereas smaller particles tend to adhere to the surface, suggesting that larger particles are less likely to settle at the bottom of the microchannel. Figure 6e illustrates the positions of particles of different sizes over time, while Figure 6b shows their velocities during sedimentation.

As shown in Figure 6b, the velocities of all particles increase during sedimentation, though their accelerations vary notably with size. Smaller particles experience a gradual decrease in acceleration, whereas larger particles exhibit a smaller reduction. Upon surface contact, particle acceleration decreases, but velocity initially rises due to contact force and gravity. As elastic forces build, the particle's velocity quickly drops and its direction reverses. The maximum velocity of larger particles is higher than that of smaller ones, which can be attributed to their greater potential energy and momentum. This is because the larger particle has a higher velocity when it contacts the surface and experiences longer acceleration due to its greater gravitational force. When the particle velocity reaches zero, the particle deformation is at its maximum, after which the particle moves upward. During this upward movement, the acceleration of the particle decreases as the elastic force caused by particle deformation diminishes. Eventually, the particle may rebound from the surface.

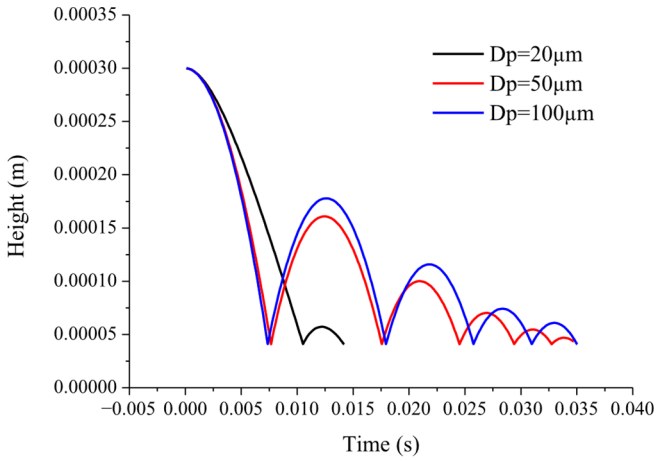

(**a**) Particle height

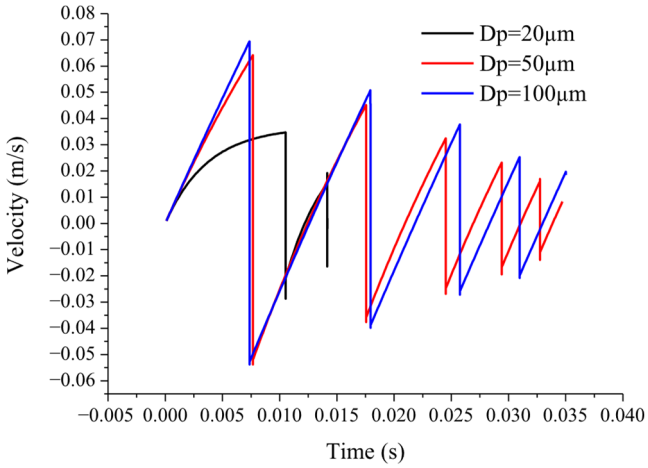

(**b**) Particle velocity

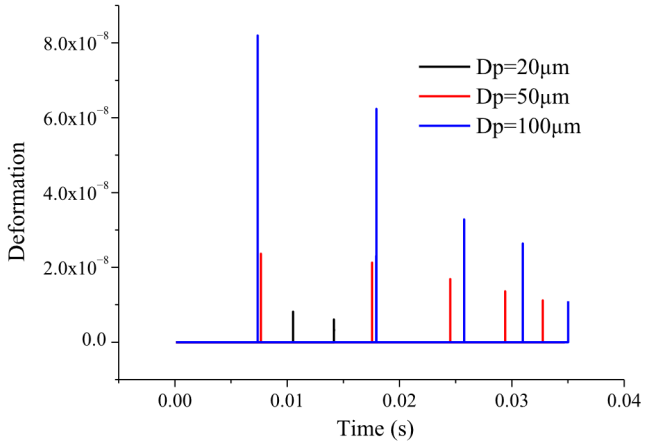

(**c**) Particle deformation

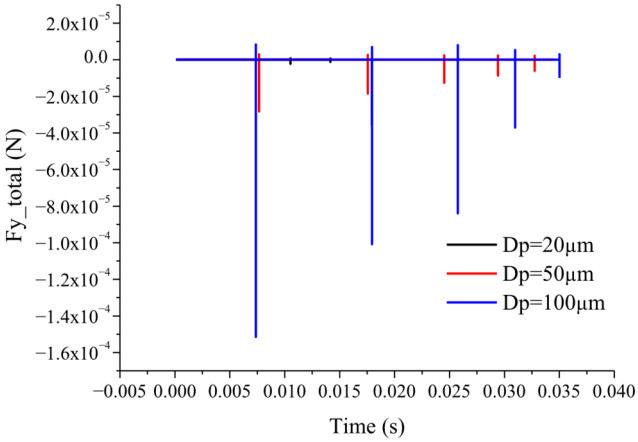

(**d**) Force exerted on the particle

Figure 6. *Cont.*

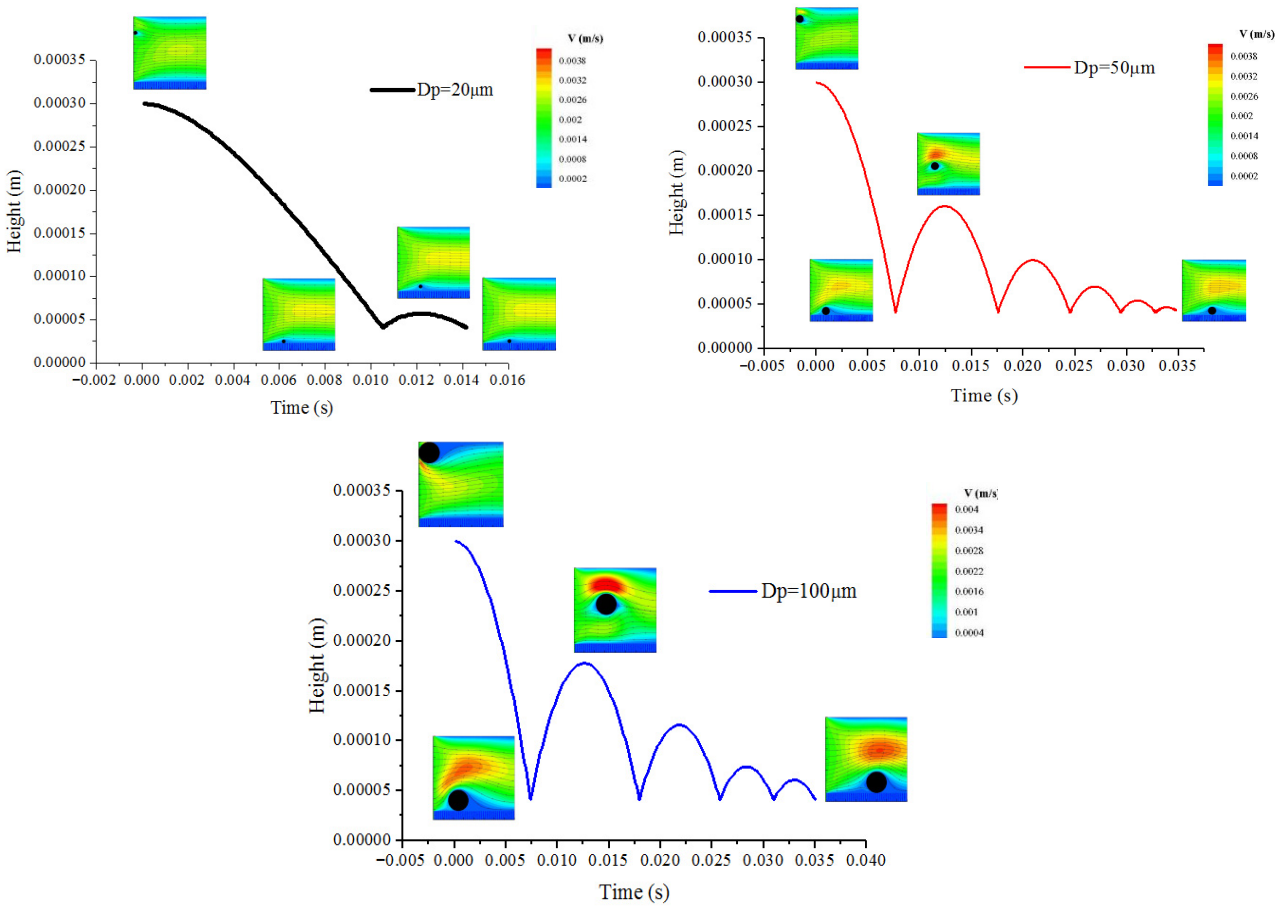

(**e**) Positions of the particle with different diameters at different time

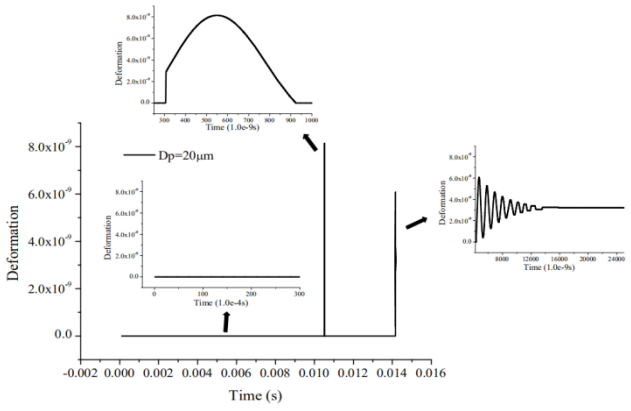

(**f**) Particle deformation at different time

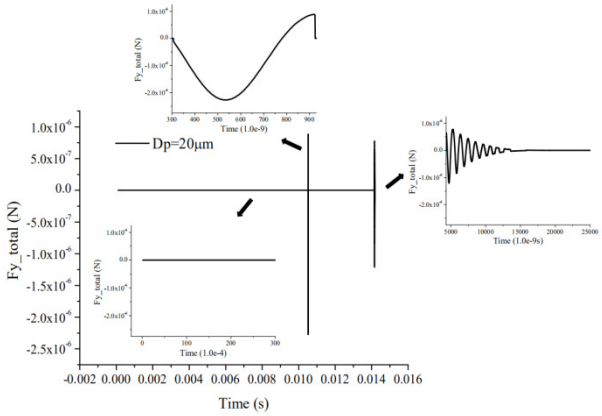

(**g**) External force on the particle

Figure 6. The velocity, height, deformation and force exerted on the particles with different diameters during the deposition process.

Figure 6c,d illustrate the particle deformation and the vertical force experienced during deposition. The contact time is much shorter than the settling time, producing peaks in both deformation and force curves. Detailed variations in particle deformation and force are discussed in the following sections. As shown in Figure 6c, larger particles undergo significantly greater deformation upon surface contact due to their higher collision velocity, which generates larger elastic forces. Figure 6d indicates that the total vertical force acting on the particle increases with particle diameter. This change in force is consistent with the changes in particle deformation. During sedimentation, the dominant forces are gravity and

drag. Upon contact with the surface, the elastic force increases due to particle deformation. The force exerted on larger particles is greater than that on smaller ones due to the larger deformation. The detailed analysis of Figure 6c,d is presented in the following sections.

For larger particles, multiple rebounds occur when they contact the surface. However, the rebound height decreases with each successive impact, while the frequency of rebounds increases. This behavior can be attributed to the combined effects of drag, contact forces, and velocity dissipation acting on the particle during deposition. Thus, the rebound height of larger particles is higher when they contact the surface, while smaller particles are more likely to adhere. These results suggest that larger particles are less likely to settle at the bottom of the microchannel. Figure 6e illustrates the positions of particles with different diameters at various time points.

Figure 6f depicts particle deformation over time, while Figure 6g presents the external forces acting on the particle during deposition. As shown in Figure 6f, larger particles experience substantially greater deformation upon surface contact compared to smaller particles. This is because the larger particle has a higher velocity upon impact, leading to greater deformation and a higher elastic force. Figure 6g indicates a positive correlation between particle diameter and the total vertical force experienced by the particle. This force variation is consistent with the changes in particle deformation. During sedimentation, gravity and drag forces dominate. However, upon surface contact, the elastic force increases due to particle deformation. The larger particle experiences a greater force than the smaller particle due to its increased deformation. The detailed analysis of Figure 6f,g is provided in the following sections.

6.2. Effects of Surface Energy

Surface energy plays a critical role in particle deposition during surface collisions. In both everyday and industrial applications, surfaces are categorized as super-hydrophilic, hydrophilic, hydrophobic, and superhydrophobic, each with a distinct contact angle [49]. Hydrophilic surfaces typically have contact angles below 30° and a surface energy of approximately 0.5 J/m^2, whereas superhydrophobic surfaces have surface energies around 0.01 J/m^2. To investigate the effect of surface energy on particle deposition, numerical simulations were conducted over a range of 0.01–0.5 J/m^2.

Figure 7 presents the particle height, velocity, deformation, and the force exerted during deposition for different surface energies. Particles adhere immediately to surfaces with higher surface energy upon contact, while they can rebound and exit the microchannel on surfaces with lower surface energy. As shown in Figure 7a, the rebound heights for surface energies of 0.01 J/m^2 and 0.05 J/m^2 are 53.65% and 38.66% of the release height, respectively. Particles remain deposited on surfaces with the highest surface energy; however, they tend to oscillate on the surface rather than detach. This oscillatory behavior results from the strong adhesive forces present on high-energy surfaces. Figure 7b indicates that the maximum particle velocity increases with surface energy, reflecting the influence of these adhesive forces.

As shown in Figure 7e, it can be seen that the particle velocity increases before it contacts the surface. After colliding with the surface, the particle will periodically move on the surface. However, the maximum velocity of the particle becomes lower. Additionally, the particle exhibits a longer oscillation period due to energy loss. As shown in Figure 7c, the particle deformation is greater when the surface energy is larger. For surface energy of 0.5 J/m^2, the particle deformation is the greatest while the particle does not rebound off the surface. This is consistent with Figure 7b. The total force acting on the particle can be found in Figure 7d. As observed, the force is much higher for higher surface energy. It is observed that surfaces with lower surface energy (characteristic of superhydrophobic

coatings) significantly enhance particle rebound. This confirms that the chemical non-affinity required for superhydrophobicity also translates to reduced work of adhesion in dry particle-wall collisions.

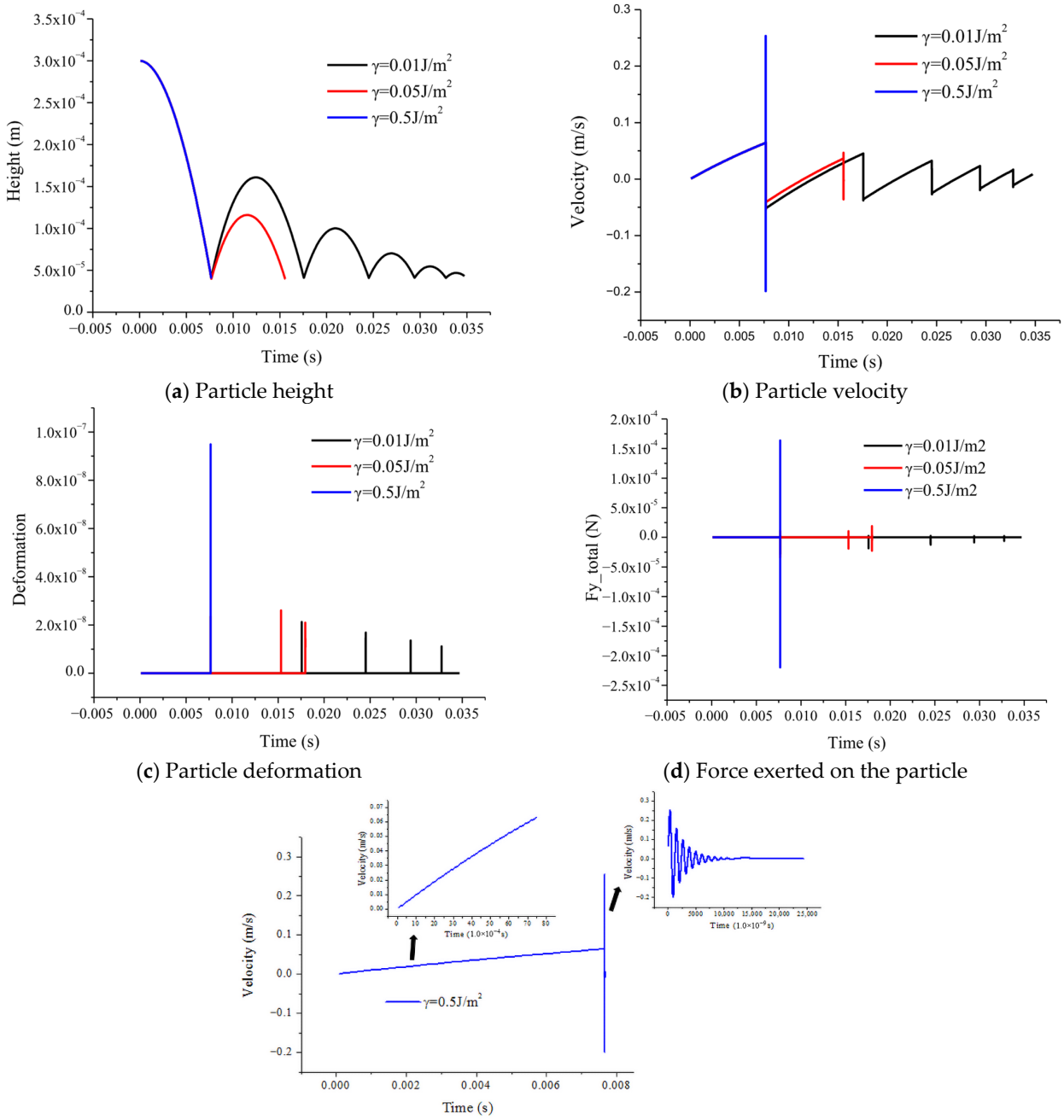

Figure 7. Velocity, height, deformation, and forces acting on particles during deposition for different surface energies.

6.3. Effects of Different Structures

Particle deposition characteristics are strongly influenced by surface structures. Therefore, investigating particle deposition behavior on different surface morphologies is essential. In the present study, a smooth surface, two types of regularly distributed rough surfaces, and three types of randomly distributed rough surfaces are examined. Figure 8 illustrates the rebound and deposition behaviors of a single particle interacting with these surfaces. It is observed that both surface roughness geometry and the presence of particles

modify local flow fields and near-wall velocity structures, which is consistent with observations reported in previous numerical studies involving particle-resolved simulations and rough or structured surfaces [6,50–52].

Figure 8a shows the flow behavior when the particle impacts the smooth surface. A relatively uniform velocity distribution of the airflow can be observed. The particle rebounds off the smooth surface and is carried away by the airflow, indicating typical deposition behavior on a smooth surface. Figure 8b depicts the flow on a surface with regularly distributed structure 1 (e/d = 1.0). Surface roughness alters the velocity distribution, causing the particle to rebound and subsequently travel with the airflow. This behavior is similar to that observed on the smooth surface but with a slight modification in airflow due to the surface structure. Figure 8c shows the flow on a surface with regularly distributed structure 2 (e/d = 0.8). As with the previous surface, the particle rebounds off the surface, but there is a noticeable change in the velocity distribution around the rough surface. The particle's motion is influenced by the regular structure, leading to differences in deposition characteristics.

As shown in Figure 8, the particle exhibits different deposition behaviors depending on the surface it collides with. When the particle impacts smooth or regularly rough surfaces, it rebounds off the surface and is carried away by the airflow. However, as shown in Figure 8e, on surfaces with randomly distributed structures, the particle may rebound off the surface and move in the opposite direction to its initial velocity. This behavior is attributed to the intrinsic characteristics of randomly distributed structures. When a particle interacts with a rough surface, the exact point of contact becomes unpredictable due to the irregular and non-uniform arrangement of the surface features, which means the contact velocity of the particle is also unpredictable. As a result, the particle may move with the airflow or in the opposite direction, as shown in Figure 8d,e. Figure 8f depicts the flow on another randomly distributed surface with skewness (Sk = 1.21) and kurtosis (K = 5.05). Similar to the behavior shown in Figure 8e, the particle undergoes oscillatory motion; however, the rebound height is greater due to the larger deformation and the unique characteristics of the surface. In this case, part of the particle's horizontal momentum is converted into vertical velocity, resulting in higher rebound heights and consequently reducing the likelihood of particle deposition.

As shown in Figure 8a, the particle on a smooth surface tends to adhere after a single contact. However, the rebound height is higher when the particle impacts the rough surface, as shown in Figure 9. This is likely attributed to the reduced effective particle–wall contact area caused by the surface roughness. Thereby decreasing the energy loss caused by the contact force. Additionally, the rough surface increases the effective contact height between the particle and the surface, which reduces energy loss due to drag. As shown in Figure 9a, the particle exhibits a higher rebound height when the surface is composed of randomly distributed structures. This indicates that surfaces with randomly distributed rough structures are more effective at increasing particle rebound height and reducing particle deposition. When the particle contacts a surface with randomly distributed structures, its horizontal velocity may be converted to vertical velocity due to the unpredictable contact position, leading to a higher rebound height. Moreover, a rough surface with Sk = 1.21 and K = 3.12 causes the particle to rebound off the surface and leave the micro-channel. Therefore, it can be concluded that rough surfaces effectively increase the rebound height of particles after collision, which reduces particle deposition in the micro-channel. Surfaces with randomly distributed structures perform better than those with regularly distributed structures.

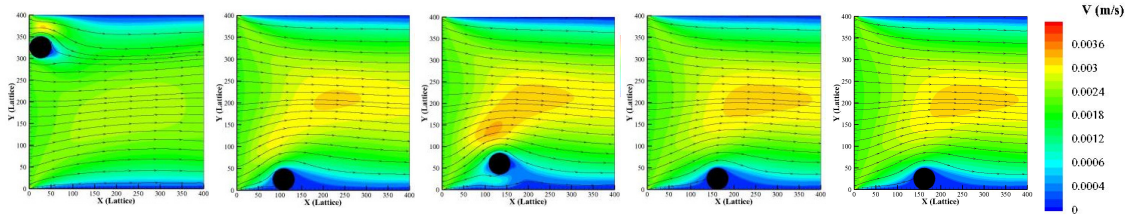

0.10 ms 8.28 ms 10.91 ms 13.59 ms 13.61 ms

(**a**) Smooth Surface

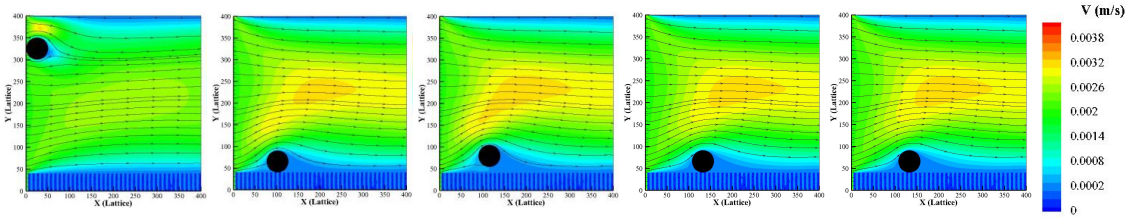

0.10 ms 7.68 ms 10.69 ms 11.03 ms 11.07 ms

(**b**) Regularly distributed structure (e/d = 1.0)

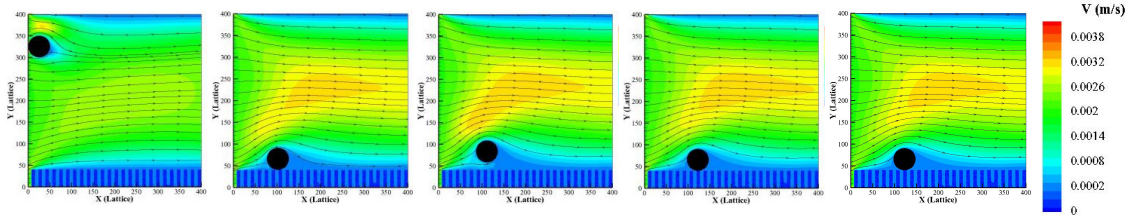

0.10 ms 7.68 ms 11.32 ms 11.59 ms 11.61 ms

(**c**) Regularly distributed structure (e/d = 0.8)

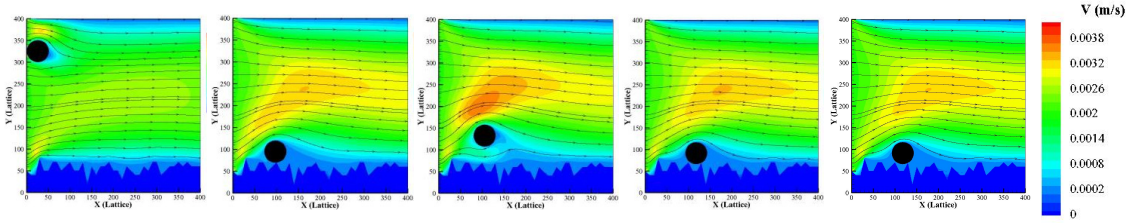

0.10 ms 7.19 ms 9.87 ms 12.79 ms 12.81 ms

(**d**) Randomly distributed structure (Sk =−0.54, K = 5.05)

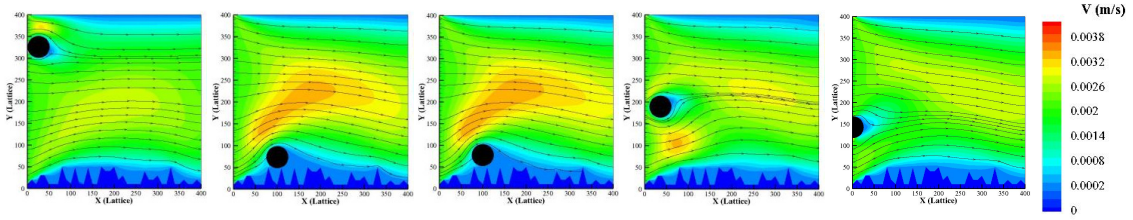

0.10 ms 7.55 ms 7.62 ms 12.26 ms 15.56 ms

(**e**) Randomly distributed structure (Sk = 1.21, K = 3.12)

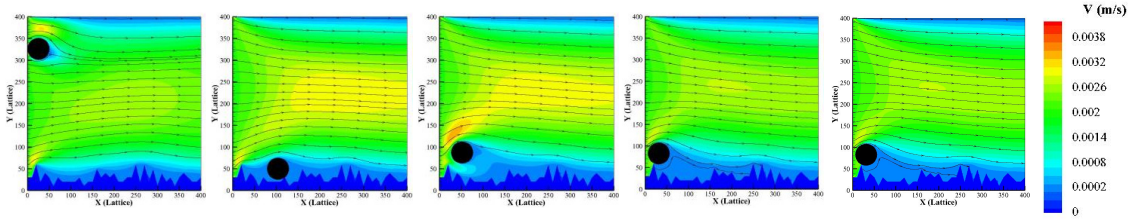

0.10 ms 7.92 ms 11.49 ms 11.63 ms 11.66 ms

(**f**) Randomly distributed structure (Sk = 1.21, K = 5.05)

Figure 8. Flow of the micro-channel during the particle deposition on different surfaces.

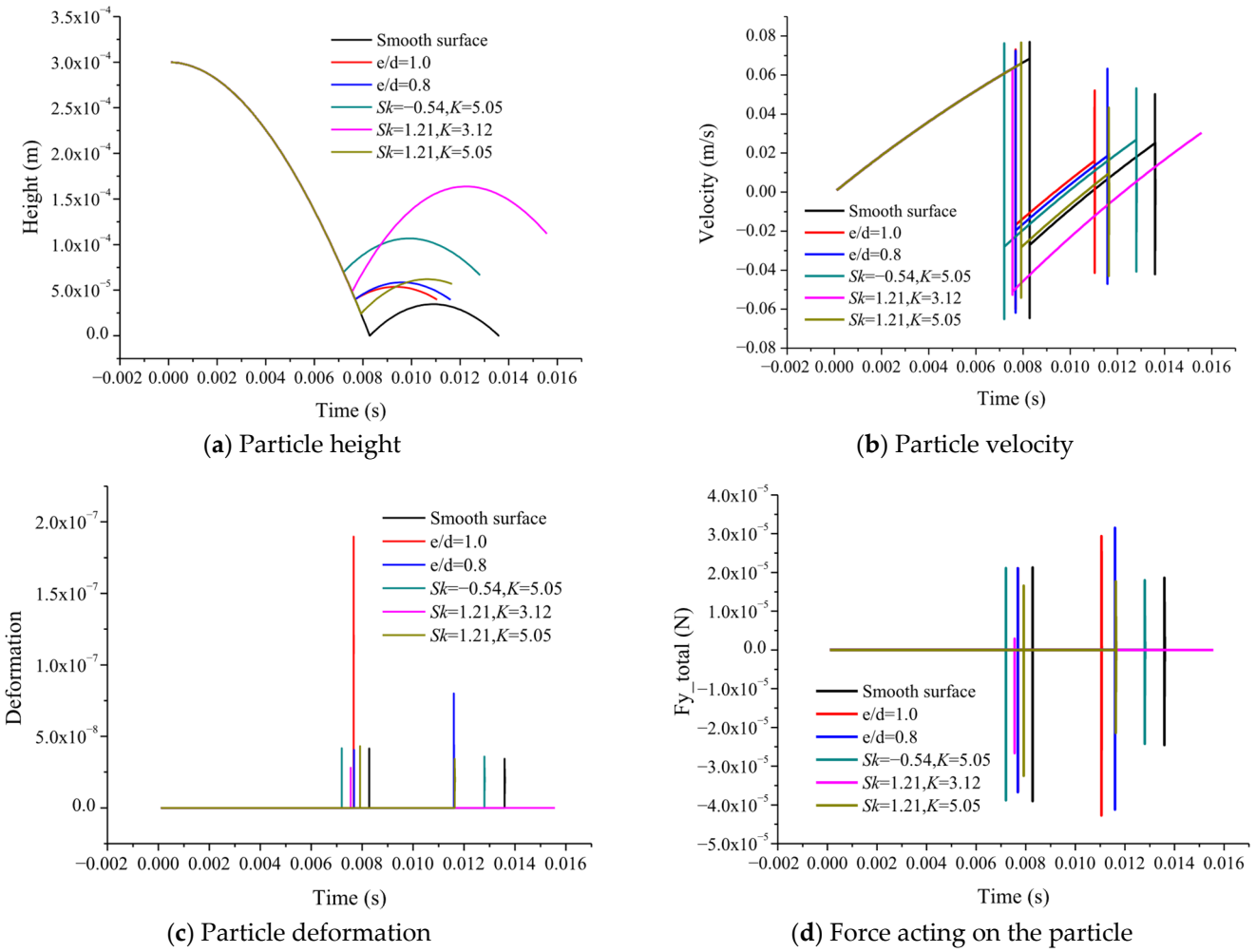

Figure 9. Velocity, particle height, deformation and force during deposition on different surfaces.

Figure 9b presents the particle velocity changes over time for different surfaces. The velocity decreases more rapidly on smooth surfaces due to the higher adhesion forces; in contrast, on rough surfaces, especially those exhibiting random distributions, the velocity remains higher and can even reverse direction. Figure 9c shows the particle deformation over time. The deformation is greater for rough surfaces, as the increased velocity at impact causes larger forces, leading to more significant deformation. In Figure 9d, the force exerted on the particle in the vertical direction is displayed. The force peak may increase due to localized asperity contact and impact reorientation, which helps propel the particle upward, resulting in higher rebound heights, as seen in Figure 9a.

It is also worth noting that the current contact model focuses on normal interactions and neglects tangential friction and particle rotation. For the micron-sized adhesive particles (20–100 μm) investigated in this study, the collision dynamics are primarily dominated by the interplay between van der Waals adhesive forces and elastic deformation in the normal direction. Previous studies have also indicated that particle sliding is rare for small adhesive particles during the brief impact duration. However, the exclusion of frictional dissipation and rotational energy transfer may lead to a conservative estimation of energy loss. Consequently, the predicted rebound heights presented in Figure 9 likely represent an upper bound compared to experimental scenarios where tangential damping is present. Despite this, the relative trends observed, specifically that random roughness suppresses deposition more effectively than regular roughness by reducing the effective contact area,

remain valid and are governed primarily by the geometric features of the surface rather than frictional effects.

6.4. Effects of the Young's Modulus

The Young's modulus of a particle is an important factor in determining its hardness and elasticity. Particles with a higher Young's modulus are more resistant to deformation. Real airborne particles exhibit a wide range of Young's modulus values, typically ranging from 50 to 400 MPa. The Young's modulus of soil is around 50–75 MPa, while that of sand is approximately 150 MPa. To assess the impact of Young's modulus on deposition behavior, values of 50, 200, and 400 MPa were selected. The corresponding particle height, velocity, deformation, and forces are shown in Figure 10.

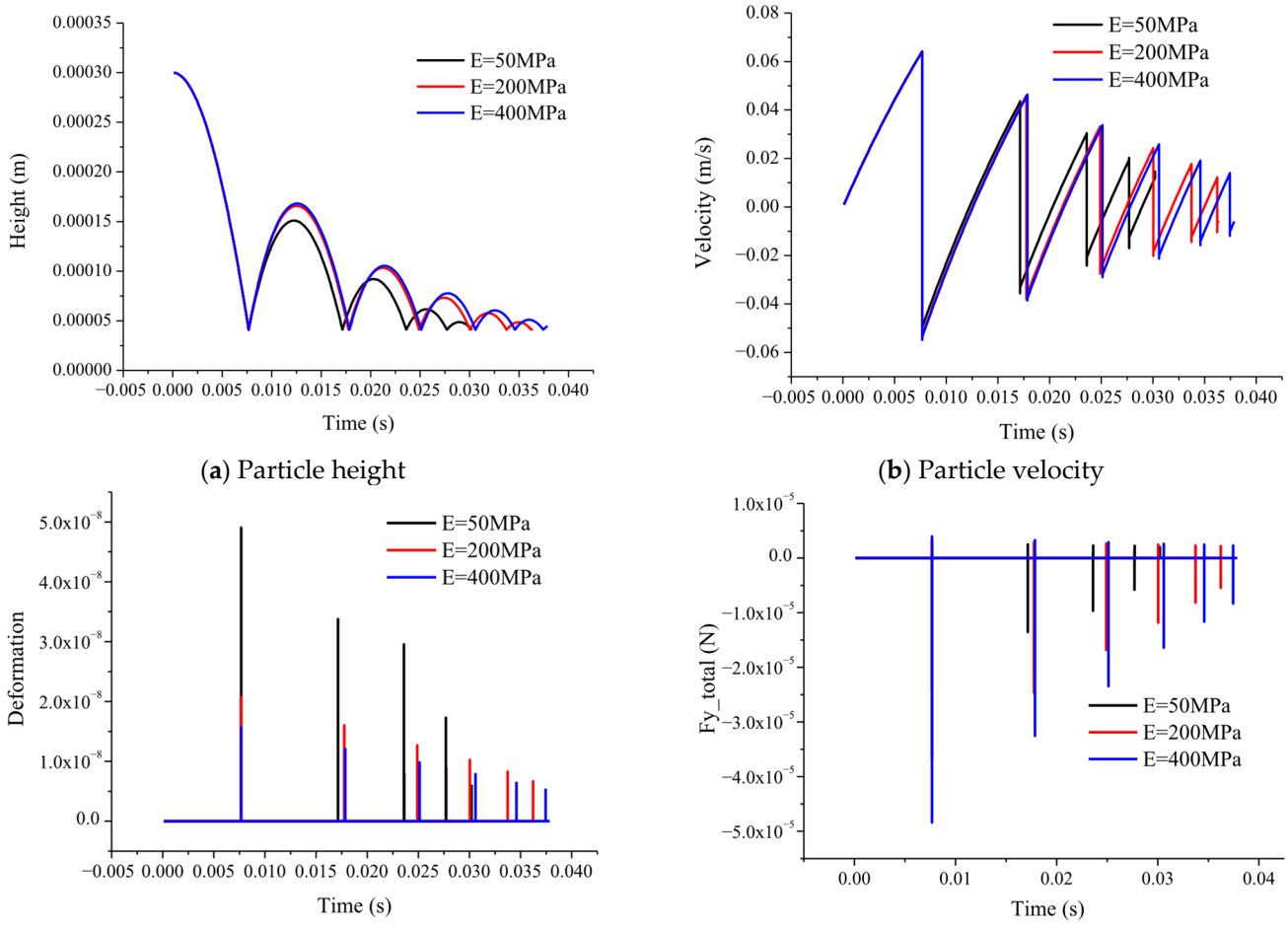

(**a**) Particle height (**b**) Particle velocity

(**c**) Particle deformation (**d**) Force exerted on the particle

Figure 10. The velocity, height, deformation and force exerted on the particle with different Young's modulus during the deposition process.

Figure 10a shows that particles with higher Young's modulus achieve greater rebound, with normalized heights of 50.3%, 55.3%, and 56.1% for 50 MPa, 200 MPa, and 400 MPa, respectively, on regularly structured surfaces. Particles with lower modulus exhibit little change after multiple impacts, making them more prone to settle in the microchannel. Figure 10b illustrates particle velocity over time, indicating that stiffer particles undergo more pronounced velocity variations upon collision. The variation in particle velocity for different Young's moduli follows a similar trend to that observed in the previous section, so it will not be discussed in detail here. Particles with higher Young's modulus reach greater maximum velocities due to the larger elastic forces they generate. As shown in Figure 10d,

the force acting on the particle also increases with increasing Young's modulus. Figure 10c displays the change in particle deformation over time. The analysis of particle deformation and the corresponding forces is not detailed here. Particles with lower Young's modulus are more prone to deformation, resulting in larger maximum deformation compared to stiffer particles. Consequently, Young's modulus affects both rebound height and peak velocity. Particles with smaller modulus are more likely to settle in the microchannel.

To evaluate the transition between inertia-dominated impact and fluid-controlled deposition, a dimensionless energy comparison was conducted.

6.5. Effects Comparison Between the Particle Diameter, Young's Modulus and Surface Energy

Particle rebound height upon surface impact is influenced by diameter, Young's modulus, and surface energy. The following analysis compares how these parameters affect particle deposition behavior. Figure 11 illustrates the highest rebound height for particles with different parameters when they deposit on the surface. The vertical axis represents the ratio of the highest rebound height to the initial release height. It is evident that particle diameter has a more significant influence on particle deposition behavior compared to the other parameters. In the computational case, for particles contacting surfaces with regularly distributed structures, when the particle diameter increases from 20 μm to 100 μm (five times larger), the highest rebound height increases by a factor of 2.1 compared to the smaller particle. Additionally, the influence of particle diameter on rebound height decreases as diameter increases, indicating a nonlinear relationship between size and rebound. For Young's modulus, although the value increases eightfold from 50 MPa to 400 MPa, the maximum rebound height increases by only 0.2 times. As shown in Figure 11b, the change in rebound height is not linear with respect to Young's modulus. For surface energy, when the surface energy decreases from 0.05 J/m^2 to 0.01 J/m^2 (a 5-fold decrease), the highest rebound height increases by 0.4 times. Therefore, it can be concluded that particle diameter has a more pronounced effect on rebound height compared to the other parameters.

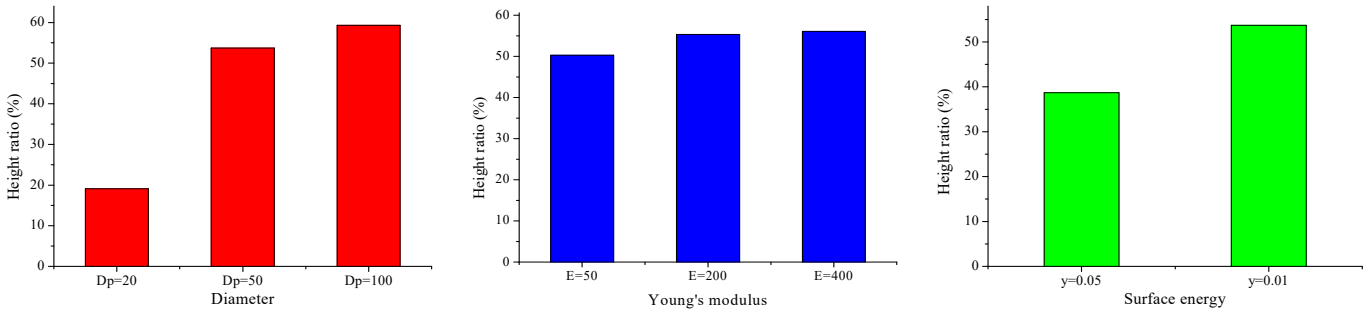

(**a**) Effects of diameter (**b**) Effects of Young's modulus (**c**) Effects of Surface energy

Figure 11. The effects comparison between the particle diameter, Young's modulus and Surface energy.

It should be noted that the conclusions of this study primarily apply to rigid particles. For highly compliant particles such as bioaerosols or polymers, their low Young's modulus may induce 'conformal contact,' transforming the contact mechanism from multipoint contact to near-surface contact. This significantly enhances adhesion and energy dissipation. In such cases, Young's modulus may become the dominant factor influencing sedimentation behavior.

6.6. Effects of the Flow Reynolds Number on Particle Deposition Behavior

The influence of flow Reynolds number on particle deposition was examined in this study. The Reynolds number is defined based on the particle diameter and the mean inlet velocity. As shown in Figure 12, particles remain in the channel for a shorter duration at higher Reynolds numbers, as the faster flow tends to carry them away. Figure 13a shows that while the rebound height decreases with increasing Reynolds number, the particle is still able to exit the channel. Additionally, higher Reynolds numbers correspond to increased horizontal particle velocity. Upon collision with the surface, the particle undergoes greater deformation, and more energy is lost, which results in a reduced rebound height. Figure 13b shows that the particle velocity may be lower when the Reynolds number is higher, which is consistent with the observation in Figure 12a. Figure 12c,d present the particle deformation and total force during deposition. Higher Reynolds numbers result in increased deformation and greater forces acting on the particle, providing a physical explanation for the observed reduction in rebound height. Therefore, it can be concluded that particles are less likely to deposit on the surface when the Reynolds number is high. Additionally, under higher Reynolds numbers, the particle may only collide with the superhydrophobic surface once. To reduce particle deposition at the bottom of the micro-channel, increasing the flow Reynolds number is an effective method.

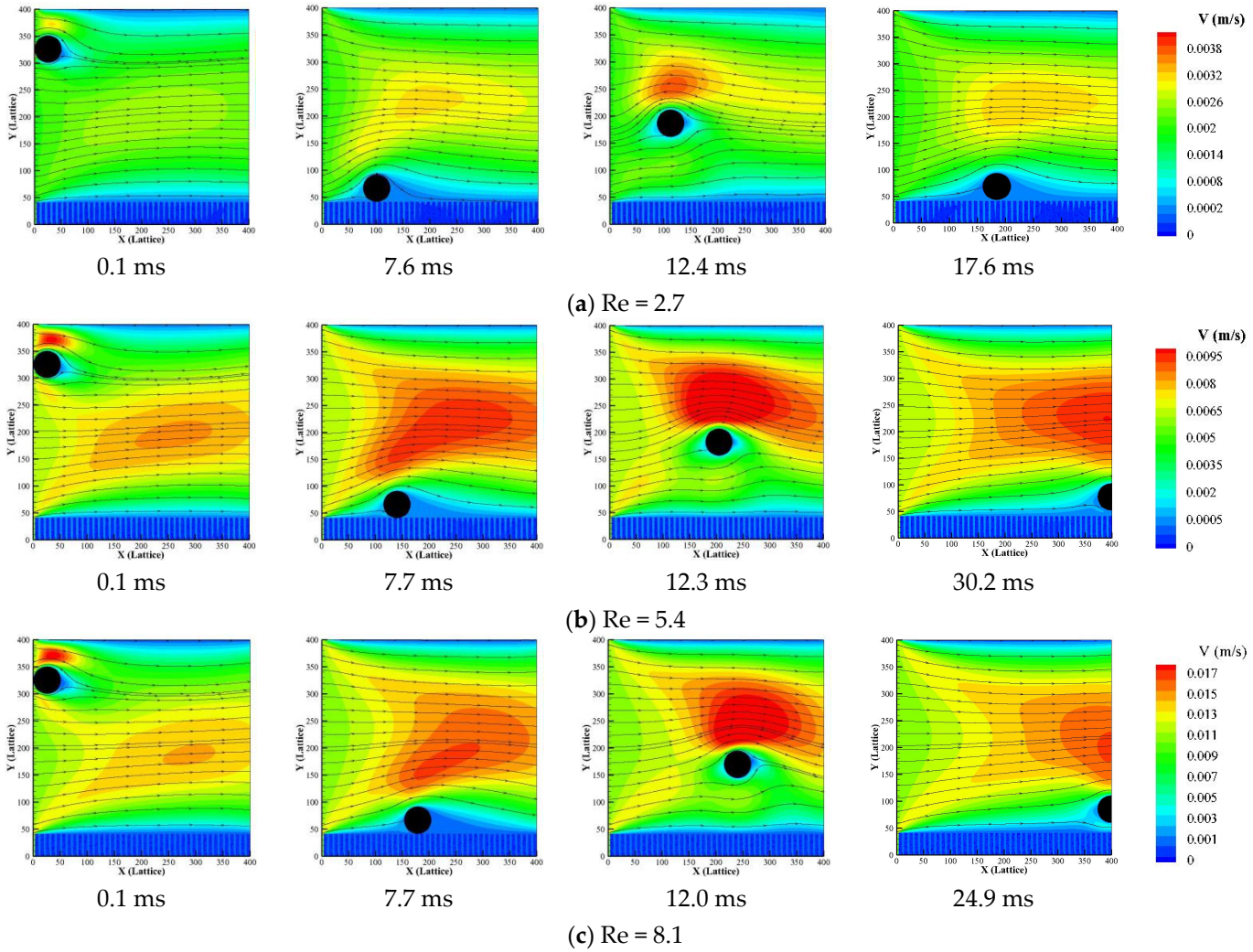

Figure 12. Flow of the micro-channel during the particle deposition with different Reynolds numbers.

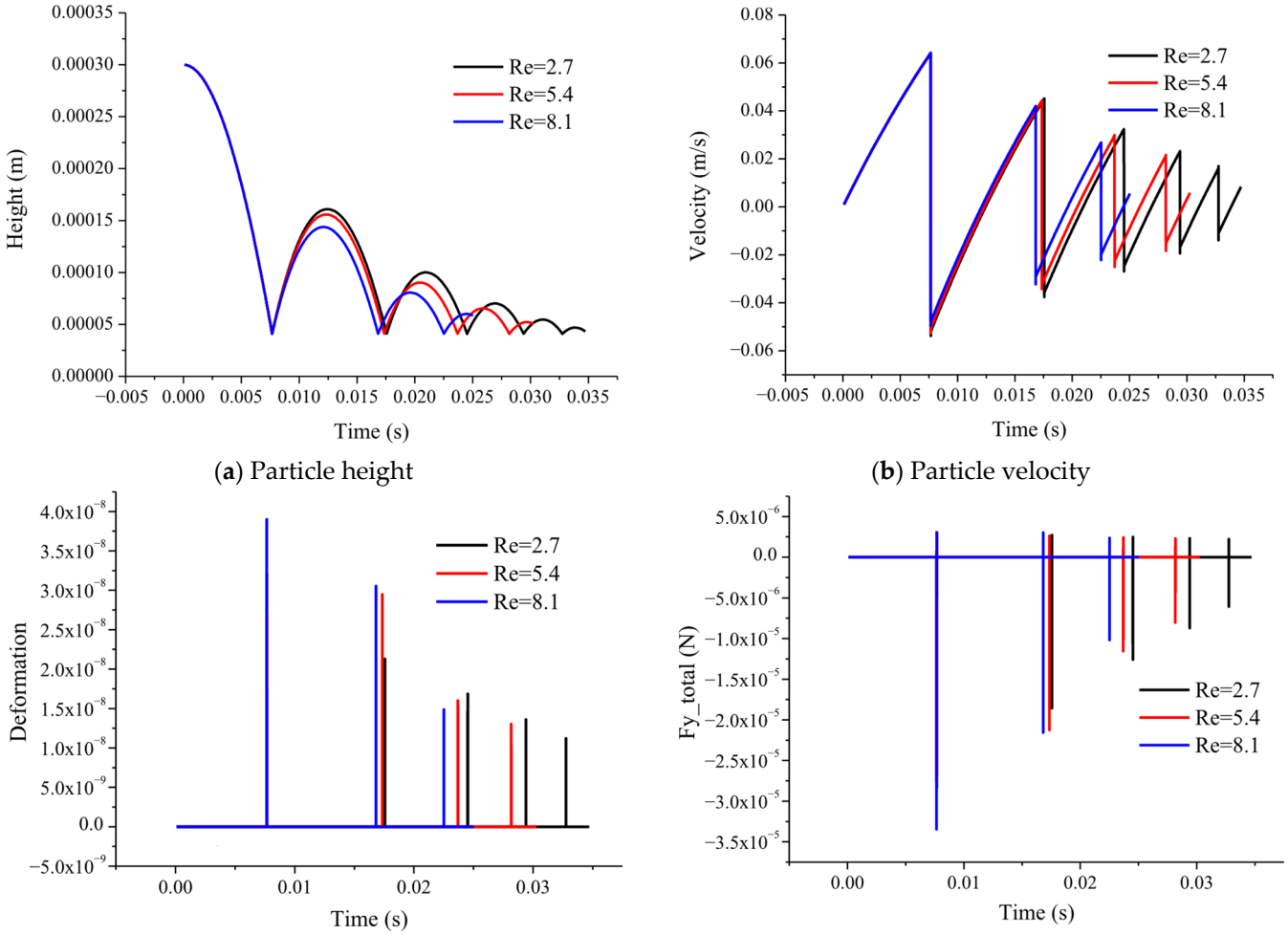

(**a**) Particle height (**b**) Particle velocity

(**c**) Particle deformation (**d**) Force acting on the particle

Figure 13. The velocity, height, deformation and force exerted on the particle with different flow Reynolds numbers.

To evaluate the transition between inertia-dominated impact and fluid-controlled deposition, a dimensionless energy comparison was conducted. The formula for the ratio of particle kinetic energy to adhesive work is:

$$\begin{cases} E_k = \frac{1}{2} m_p {u_p}^2 \\ W_{adh} = \gamma A_c \\ \Pi_1 = \frac{E_k}{W_{adh}} \end{cases} \tag{36}$$

where E_k is the particle's kinetic energy before impact. m_p is the particle mass. u_p is the particle center velocity. $\mathrm{W_{adh}}$ is the energy required to overcome adhesion. γ is the surface energy. A_c is the contact area between the particle and the surface. Π_1 is the ratio of particle kinetic energy to adhesion work.

The formula for the ratio of fluid drag work to kinetic energy is:

$$\begin{cases} W_d = F_d g L \\ \Pi_2 = \frac{W_d}{E_k} \end{cases} \tag{37}$$

where W_d is the work done by fluid resistance on particles. F_d is the fluid drag force. g is gravitational acceleration. L is the characteristic drag path length. Π_2 is the ratio of the work done by fluid resistance on a particle to the particle's kinetic energy.

When $\Pi_2 < 1$, adhesive forces exceed particle inertia, promoting deposition. When $\Pi_2 > 1$, viscous dissipation effects surpass collision energy, indicating fluid action becomes the dominant factor controlling particle motion. This transition roughly corresponds to the low Stokes number region, demonstrating that when viscous effects suppress particle inertia, fluid forces begin to dominate. The reduced rebound height and increased deformation observed at higher Reynolds numbers align with this transition: although the initial kinetic energy E_k increases ($\Pi_1 > 1$), establishing shock-dominated conditions, the fluid resistance work W_d also increases significantly ($\Pi_2 \approx 1$). This causes most of the initial energy to be dissipated by the fluid during the collision, reducing g the actual energy available for elastic rebound. Consequently, the rebound height decreases.

7. Conclusions

This study investigates the deposition, rebound, and adhesion behavior of a single particle impacting rough superhydrophobic surfaces. Randomly distributed rough surfaces were reconstructed using a Fast Fourier Transform (FFT) approach, and a coupled Lattice Boltzmann Method (LBM) and Discrete Particle Model (DPM) framework was employed to resolve particle transport and collision dynamics. A new particle–surface contact model was developed to account for adhesion, elastic deformation, and localized roughness effects for both regularly and randomly structured surfaces. The numerical model was validated against single-particle impact experiments, and the effects of particle properties, surface characteristics, and flow conditions on deposition behavior were systematically examined. The main conclusions are summarized as follows:

1. The proposed particle–surface contact model shows good agreement with experimental measurements, demonstrating its capability to reliably predict particle deposition and rebound behavior on rough surfaces.
2. Superhydrophobic surfaces significantly enhance particle rebound after impact, thereby reducing particle deposition. Compared with regularly structured surfaces, randomly distributed rough surfaces are more effective in promoting particle rebound and detachment.
3. Deposited particles exhibit periodic wall-normal oscillations rather than remaining stationary. During successive oscillations, particle velocity decreases, oscillation periods increase, and peak deformation induced by adhesive interactions with surface roughness gradually diminishes.
4. Particle deposition behavior is strongly influenced by particle diameter, Young's modulus, surface energy, and flow Reynolds number. Larger particles achieve higher rebound heights, whereas smaller particles are more prone to adhesion. Higher surface energy enhances particle adhesion, whereas low-energy surfaces facilitate particle rebound.
5. Among the investigated parameters, particle diameter is identified as the dominant factor governing rebound behavior. Increasing particle diameter by a factor of five results in a 2.1-fold increase in maximum rebound height, whereas an eightfold increase in Young's modulus leads to only a 0.2-fold increase. Similarly, reducing surface energy to one-fifth of its original value yields a comparatively modest increase in rebound height. The dependence of rebound height on particle diameter and Young's modulus is nonlinear.

The present work provides detailed insight into single-particle deposition mechanisms on rough superhydrophobic surfaces. Interactions among multiple particles were not considered and will be addressed in future studies to extend the applicability of the proposed model to more realistic particulate systems. Furthermore, the model's validation could be extended by incorporating more complex surface morphologies, such as hierarchical or

anisotropic structures, and by improving experimental statistics through a broader range of surface types and particle sizes.

Author Contributions: Methodology, W.Z.; Software, W.Z.; Validation, H.L.; Investigation, W.Z.; Writing—original draft, W.Z.; Writing—review & editing, H.L.; Supervision, H.L.; Project administration, H.L.; Funding acquisition, H.L. All authors have read and agreed to the published version of the manuscript.

Funding: This research was funded by the Tianshan Talent Innovation Team Project of Xinjiang (2023TSYCTD0009).

Institutional Review Board Statement: Not applicable.

Informed Consent Statement: Not applicable.

Data Availability Statement: The original contributions presented in this study are included in the article. Further inquiries can be directed to the corresponding author.

Conflicts of Interest: The authors declare no conflict of interest.

Nomenclature

Latin letters

Symbol	Definition	Unit
a_0	Equilibrium contact area radius	m
A_c	Contact area	m^2
C_c	Cunningham slip correction factor	-
C_d	Drag coefficient	-
d_p	Particle diameter	m
E	Young's modulus	Pa
E_k	Particle kinetic energy before impact	J
F	Total force	N
F_c	Critical Force	N
F_d	Fluid drag force	N
F_n	Contact force	N
F_{nd}	Dissipation force	N
F_{ne}	Elastic force	N
F_t	Additional external force	N
$f_i(x,t)$	Fluid density distribution function	-
$f_i^{eq}(x,t)$	Equilibrium distribution function	-
g	Gravitational acceleration	m/s^2
$H(I,J)$	Transfer function	-
$h(k,j)$	filter function	-
K	Kurtosis	-
k_N	Normal elastic stiffness	N/m
K_n	Knudsen number	-
L	Path Length of Resistance Effect	m
m_p	Particle mass	kg
M, N	Number of surface mesh nodes	-
N_t	Number of contact nodes	-
Re_p	Particle Reynolds number	-
R_q	Root Mean Square Roughness	μm
R_z	Autocorrelation function	-
S	Density ratio of the particle to the fluid	-
Sk	skewness	-
Sz, S_η	Probability density function	-
u_g	Fluid velocity	m/s

u_p	Particle center velocity	m/s
v_p	Particle relative velocity	m/s
W_{adh}	Energy required to overcome adhesion	J
W_d	Work done by fluid resistance on particles	J
X_p	Position of the particle center	-
$z(I, j)$	Height arrays	-
Greek letters		
Symbol	Definition	Unit
α	Coefficient of friction	-
β_x, β_y	Autocorrelation length in the x and y directions	m
γ	Surface energy	J/m^2
δ_n	Normal overlap quantity	m
δ_c	Critical overlap amount	m
$\eta(i, j)$	Enter a random sequence	-
η_n	Dissipation coefficient	kg/s
λ	Average free path of air molecules	m
μ	Fluid viscosity	Pa·s
ρ	Fluid density	kg/m^3
τ	Particle relaxation time	s
w_i	LBM Weighting Coefficient	-
Π_1, Π_2	Energy Ratio	-

References

1. Hong, W.; Wang, B.; Liu, Y.; Li, H. Numerical study of the fine particle deposition behaviors on three-dimensional random rough walls. *Powder Technol.* **2020**, *375*, 233–243. [CrossRef]
2. Zhou, L.; Zhang, X.; Yu, Y. Experimental and numerical studies on the wall-roughness effect to particle dynamics in various gas-particle flows. *Exp. Comput. Multiph. Flow* **2024**, *6*, 387–394. [CrossRef]
3. Wang, Y.; Peng, H.; Yin, Z.; Bao, F.; Hou, L. Deposition characteristics of ultrafine particles of different shapes in an inertial impactor: CFD–DEM simulations and experiments. *Exp. Comput. Multiph. Flow* **2025**, *7*, 284–296. [CrossRef]
4. Yu, K.; Peng, C.; Shang, L.; Tafti, D. Elastic-plastic collision mechanism of micron-sized particle impacting rough surfaces. *Powder Technol.* **2024**, *442*, 119903. [CrossRef]
5. Doan, T.; Indraratna, B.; Nguyen, T.T.; Rujikiatkamjorn, C. Coupled CFD-DEM modelling of clogging of granular columns by cohesive fines. *Comput. Geotech.* **2025**, *177*, 106902. [CrossRef]
6. Fogouang, L.M.; André, L.; Leroy, P.; Soulaine, C. Particulate transport in porous media at pore-scale. Part 2: CFD-DEM and colloidal forces. *J. Comput. Phys.* **2024**, *519*, 113439. [CrossRef]
7. Sun, H.; Huang, L.; Long, J.; Ruan, F. CFD–DEM coupled calculation of wall wear characteristics during particles flow impacting the wall process. *Powder Technol.* **2023**, *426*, 118684. [CrossRef]
8. Zhang, H.H.; Nunayon, S.S.; Lai, A.C.K. Experimental study on deposition enhancement of ultrafine particles in a duct flow by riblets. *Appl. Therm. Eng.* **2019**, *147*, 886–894. [CrossRef]
9. Song, S.; Wang, S.; Le-Clech, P.; Shen, Y. LBM–DEM simulation of particle deposition and resuspension of pre-deposited dynamic membrane. *Powder Technol.* **2022**, *407*, 117637. [CrossRef]
10. Rousta, F.; Lessani, B.; Ahmadi, G. Particle dispersion and deposition in wall-bounded turbulent flow. *Int. J. Multiph. Flow* **2023**, *158*, 104307. [CrossRef]
11. O'Sullivan, J.J.; Espinoza, C.J.U.; Mihailova, O.; Alberini, F. Characterisation of flow behaviour and velocity induced by ultrasound using particle image velocimetry (PIV): Effect of fluid rheology, acoustic intensity and transducer tip size. *Ultrason. Sonochemistry* **2018**, *48*, 218–230. [CrossRef]
12. Sun, K.; Lu, L. Particle flow behavior of distribution and deposition throughout 90° bends: Analysis of influencing factors. *J. Aerosol Sci.* **2013**, *65*, 26–41. [CrossRef]
13. Zhao, B.; Wu, J. Particle deposition in indoor environments: Analysis of influencing factors. *J. Hazard. Mater.* **2007**, *147*, 439–448. [CrossRef]
14. Cao, Q.; Xu, Q.Y.; Lin, C.-H.; Wei, D.; Deng, Z.; Chen, Q. Study of particle deposition on the complex components of environmental control systems. *Int. J. Heat Mass Transf.* **2019**, *135*, 1218–1232. [CrossRef]
15. Hertz, H. *Miscellaneous Papers*; Macmillan: London, UK, 1896.

16. Johnson, K.L.; Kendall, K.; Roberts, A.D. Surface energy and the contact of elastic solids. *Proc. R. Soc. Lond. A* **1971**, *324*, 301–313. [CrossRef]
17. Derjaguin, B.V.; Muller, V.M.; Toporov, Y.P. Effect of contact deformations on the adhesion of particles. *J. Colloid Interface Sci.* **1975**, *53*, 314–326. [CrossRef]
18. Almohammed, N.; Breuer, M. Modeling and simulation of particle–wall adhesion of aerosol particles in particle-laden turbulent flows. *Int. J. Multiph. Flow* **2016**, *85*, 142–156. [CrossRef]
19. Fang, Z.; Wang, H.T.; Zhang, Y.Y.; Wei, M.; Wu, X.; Sun, L. A finite element method (FEM) study on adhesive particle-wall normal collision. *J. Aerosol Sci.* **2019**, *134*, 80–94. [CrossRef]
20. Hemmati, Y.; Rafee, R. Effects of the shape and height of artificial 2D roughness elements on deposition of nano and microparticles in the turbulent gas flow inside a horizontal channel. *J. Aerosol Sci.* **2018**, *122*, 45–58. [CrossRef]
21. Kartushinsky, A.; Tisler, S.; Oliveira, J.G.; van der Geld, C.W.M. Eulerian-Eulerian modelling of particle-laden two-phase flow. *Powder Technol.* **2016**, *301*, 999–1007. [CrossRef]
22. Li, J.; Xu, Z.; Han, Z. A particle deposition model considering particle size distribution based on the Eulerian approach. *Powder Technol.* **2023**, *427*, 118759. [CrossRef]
23. Gong, T.; Zhou, Y.; Ma, Z.; Yang, W.; Tang, X.; Zhang, Q. Regulation mechanism of wall roughness on micron-sized particle deposition in pneumatic conveying bend pipes. *Phys. Fluids* **2025**, *37*, 083338. [CrossRef]
24. Abbasi, S.; Mehdizadeh, A. On the interplay between fluid flow characteristics and small particle deposition in turbulent wall bounded flows. *Phys. Fluids* **2024**, *36*, 113305. [CrossRef]
25. Ahmadian, M.H.; Zheng, W. Simulating the fluid–solid interaction of irregularly shaped particles using the LBM-DEM coupling method. *Comput. Geotech.* **2024**, *171*, 106395. [CrossRef]
26. Li, L.; Xu, P.; Li, Q.; Zheng, R.; Xu, X.; Wu, J.; He, B.; Bao, J.; Tan, D. A coupled LBM-LES-DEM particle flow modeling for microfluidic chip and ultrasonic-based particle aggregation control method. *Appl. Math. Model.* **2025**, *143*, 116025. [CrossRef]
27. Xia, M.; Fu, J.; Feng, Y.T.; Gong, F.; Yu, J. A particle-resolved heat–particle–fluid coupling model by DEM–IMB–LBM. *J. Rock Mech. Geotech. Eng.* **2024**, *16*, 2267–2281. [CrossRef]
28. Liu, S.; Liu, X.; Latthe, S.S.; Gao, L.; An, S.; Yoon, S.S.; Liu, B.; Xing, R. Self-cleaning transparent superhydrophobic coatings through simple sol–gel processing of fluoroalkylsilane. *Appl. Surf. Sci.* **2015**, *351*, 897–903. [CrossRef]
29. Pan, A.J.; Lu, H.; Zhang, L.-Z. Experimental investigation of dust deposition reduction on solar cell covering glass by different self-cleaning coatings. *Energy* **2019**, *181*, 645–653. [CrossRef]
30. Zhang, L.-Z.; Pan, A.-J.; Cai, R.-R.; Lu, H. Indoor experiments of dust deposition reduction on solar cell covering glass by transparent super-hydrophobic coating with different tilt angles. *Sol. Energy* **2019**, *188*, 1146–1155. [CrossRef]
31. Pastewka, L.; Robbins, M.O. Contact between rough surfaces and a criterion for macroscopic adhesion. *Proc. Natl. Acad. Sci. USA* **2014**, *111*, 3298–3303. [CrossRef] [PubMed]
32. Müser, M.H.; Dapp, W.B.; Bugnicourt, R.; Sainsot, P.; Lesare, N.; Lubrecht, T.A.; Persson, B.N.J.; Harris, K.; Bennett, A.; Schulze, K.; et al. Meeting the contact-mechanics challenge of rough surfaces. *Tribol. Lett.* **2017**, *65*, 118. [CrossRef]
33. Wang, S. Effects of Surface Roughness on the Indoor Particle Deposition Rate Constant. Ph.D. Thesis, Syracuse University, Syracuse, NY, USA, 2012.
34. Muller, V.M.; Yushchenko, V.S.; Derjaguin, B.V. On the influence of molecular forces on the deformation of an elastic sphere and its sticking to a rigid plane. *J. Colloid Interface Sci.* **1980**, *77*, 91–101. [CrossRef]
35. Maugis, D. Adhesion of spheres: The JKR–DMT transition using a Dugdale model. *J. Colloid Interface Sci.* **1992**, *150*, 243–269. [CrossRef]
36. Sefene, E.M.; Chen, C.-C.A.; Wang, S.H.-M. Determination of sawing temperature in multi-diamond wire sawing of mono-crystalline silicon carbide. *CIRP J. Manuf. Sci. Technol.* **2025**, *60*, 38–55. [CrossRef]
37. Davies, C.N. Definitive equations for the fluid resistance of spheres. *Proc. Phys. Soc.* **1945**, *57*, 259–270. [CrossRef]
38. Lu, H.; Zhao, W.J. Effects of particle sizes and tilt angles on dust deposition characteristics of a ground-mounted solar photovoltaic system. *Appl. Energy* **2018**, *220*, 514–526. [CrossRef]
39. Cai, R.-R.; Lu, H.; Zhang, L.-Z. Evaluation the effect of fiber alignment on particle collection performance of mechanical/electret filters based on Voronoi tessellations. *Chem. Eng. Sci.* **2019**, *197*, 109–119. [CrossRef]
40. Li, S.; Marshall, J.S.; Liu, G.; Yao, Q. Adhesive particulate flow: The discrete-element method and its application in energy and environmental engineering. *Prog. Energy Combust. Sci.* **2011**, *37*, 633–668. [CrossRef]
41. Wu, J.-J. Simulation of rough surfaces with FFT. *Tribol. Int.* **2000**, *33*, 47–58. [CrossRef]
42. Wu, J.-J. Simulation of non-Gaussian surfaces with FFT. *Tribol. Int.* **2004**, *37*, 339–346. [CrossRef]
43. Manesh, K.K.; Ramamoorthy, B.; Singaperumal, M. Numerical generation of anisotropic 3D non-Gaussian engineering surfaces with specified 3D surface roughness parameters. *Wear* **2010**, *268*, 1371–1379. [CrossRef]
44. Hu, Y.Z.; Tonder, K. Simulation of 3-D random rough surface by 2-D digital filter and Fourier analysis. *Int. J. Mach. Tools Manuf.* **1992**, *32*, 83–90. [CrossRef]

45. Hill, I.D.; Hill, R.; Holder, R.L. Algorithm AS 99: Fitting Johnson curves by moments. *J. R. Stat. Soc. Ser. C* **1976**, *25*, 180. [CrossRef]
46. Hill, I.D. Algorithm AS 100: Normal–Johnson and Johnson normal transformations. *J. R. Stat. Soc. Ser. C* **1976**, *25*, 190. [CrossRef]
47. Yuan, W.-Z.; Zhang, L.-Z. Lattice Boltzmann simulation of droplets impacting on superhydrophobic surfaces with randomly distributed rough structures. *Langmuir* **2016**, *33*, 820–829. [CrossRef] [PubMed]
48. Wang, F.-L.; He, Y.-L.; Tang, S.-Z.; Tong, Z.-X. Parameter study on the fouling characteristics of the H-type finned tube heat exchangers. *Int. J. Heat Mass Transf.* **2017**, *112*, 367–378. [CrossRef]
49. Jiang, Q.; Lu, H.M. Size-dependent interface energy and its application. *Surf. Sci. Rep.* **2008**, *63*, 427–464. [CrossRef]
50. Schenk, M.; García-Villalba, M.; Dušek, J.; Uhlmann, M.; Moriche, M. An immersed boundary method for particle-resolved simulations of arbitrary-shaped rigid particles. *Int. J. Multiph. Flow* **2025**, *188*, 105200. [CrossRef]
51. Powar, O.; Arun, P.A.H.; Kumar, A.M.; Kanchan, M.; Karthik, B.M.; Mangalore, P.; Santhya, M. Recent developments in the immersed boundary method for complex fluid–structure interactions: A review. *Fluids* **2025**, *10*, 134. [CrossRef]
52. Han, Z.; Lu, H. Numerical simulation of turbulent flow and particle deposition in heat transfer channels with concave dimples. *Appl. Therm. Eng.* **2023**, *230*, 120672. [CrossRef]

Disclaimer/Publisher's Note: The statements, opinions and data contained in all publications are solely those of the individual author(s) and contributor(s) and not of MDPI and/or the editor(s). MDPI and/or the editor(s) disclaim responsibility for any injury to people or property resulting from any ideas, methods, instructions or products referred to in the content.